Nanoscale

Accepted Manuscript

This article can be cited before page numbers have been issued, to do this please use: Z. Qiu, Y. Jiang, L. Li and Q. Yun, *Nanoscale*, 2026, DOI: 10.1039/D5NR05514H.

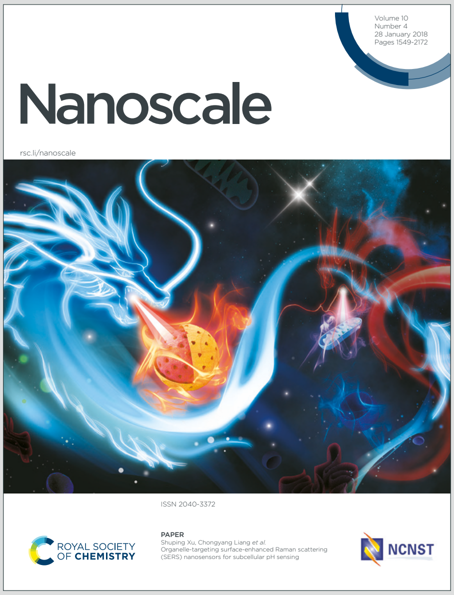

ROYAL SOCIETY OF CHEMISTRY

rsc.li/nanoscale

View Article Online
DOI: 10.1039/D5NR05514H

REVIEW

Recent Progress on Synthesis and Electrocatalytic Applications of Ni-Based Alloy Catalysts

Received 00th January 20xx,
Accepted 00th January 20xx

DOI: 10.1039/x0xx00000x

Zhongjie Qiu,[†a] Yuan Jiang,[†a] Lei Li,[*a] and Qinbai Yun[*a]

Ni-based alloys represent a significant class of non-precious metal electrocatalysts, featured with tunable compositions, favorable electronic properties, and excellent chemical stability in alkaline media. Introducing a secondary element into Ni alters its electronic structure and surface coordination environment, thereby modulating the adsorption behavior of key reaction intermediates and enhancing overall catalytic performance. Recent studies demonstrate the effectiveness of this alloying strategy across a broad range of electrocatalytic reactions. This review summarizes the synthesis and applications of Ni-based alloy catalysts in electrochemical energy production and conversion. Synthesis methods for various Ni-based alloy electrocatalysts are discussed, including thermal treatment, liquid-phase synthesis, and vapor-phase synthesis approaches. The applications of Ni-based catalysts in diverse electrocatalytic processes are summarized, including hydrogen oxidation, hydrogen evolution, oxygen evolution, oxygen reduction, and CO_2 reduction reactions. The mechanisms underlying these processes are analyzed, especially the factors influencing their activity and selectivity. Particular attention is given to the correlations between alloy composition, structural features, and catalytic behavior. Finally, remaining challenges related to active site identification, stability under operational conditions, and scalable synthesis are discussed, along with prospects for future research on Ni-based alloy electrocatalysts.

1. Introduction

Energy serves as a vital driving force for societal development. The exploration and utilization of fossil fuels have significantly transformed production methods and propelled human progress. However, fossil fuel reserves are finite, and their excessive consumption has triggered multiple ecological crises, including global warming, acid rain, and air pollution, severely hindering the achievement of carbon peak and carbon neutrality goals and constraining the sustainable development of human society.[1, 2] Therefore, there is an urgent need to establish sustainable methods that do not rely on fossil fuels to produce the fuels and high-value-added chemicals required by human society.[3] Electrochemical energy conversion technologies, including water electrolysis, metal-air batteries, fuel cells, and electrocatalytic carbon dioxide reduction, play an increasingly critical role in green energy systems.[4] On one hand, electrical energy can be sourced from renewable resources such as solar, wind, and tidal power. On the other hand, electrocatalytic technologies enable the conversion of naturally occurring small molecules, such as water, oxygen, and carbon dioxide, into high-value fuels and chemicals.[5] Furthermore, direct modulation of electrocatalytic reaction kinetics via voltage adjustment enables safe and flexible control over product selectivity.[6-8] The key step in achieving efficient electrocatalysis lies in developing electrocatalysts that combine high activity with high selectivity to achieve the desired chemical transformation.

Currently, while traditional precious metal catalysts (such as Pt, Ir, and Ru) exhibit outstanding performance in most reactions,[8] their scarcity and high cost, coupled with unsatisfied stability, limit their large-scale application.[9] In contrast, non-noble metal-based materials are regarded as a promising alternative system due to their abundant resources, low cost, diverse structures, and tunable electronic properties.[10, 11] Ni has garnered significant attention as an electrocatalyst owing to its high natural abundance (the fourth most abundant transition metal globally), low cost (one-two thousandth the price of Pt), high electrical conductivity, corrosion resistance, and excellent stability in alkaline environments.[12-18] Moreover, its catalytic performance can be further optimized by regulating its oxidation state, coordination environment, and crystal structure.[19] It possesses electronic properties similar to those of Pd or Pt, enabling it to catalyze many of the same fundamental reactions, and finds extensive application in the field of electrochemistry.[15]

However, the electrocatalytic activity of Ni alone remains unsatisfactory and requires further optimization.[20] To achieve practical applications, efforts must be devoted to adjusting the local environment and electronic structure of Ni to enhance its catalytic activity and stability. Specifically, introducing other metallic or non-metallic elements into Ni lattice to form Ni-based alloys offers additional possibilities for regulating their surface properties.[21] Moreover, Ni exhibits high alloying

---

[a] Sustainable Energy and Environment Thrust, The Hong Kong University of Science and Technology (Guangzhou), Nansha, Guangzhou 511400, China.
E-mail: qinbaiyun@hkust-gz.edu.cn (Q. Yun), ll@hkust-gz.edu.cn (L. Li).

† These authors contributed equally to this work.

Qinbai Yun and Lei Li are co-corresponding authors of this work.

efficiency with other metals, facilitating the development of a diverse range of Ni-based alloy catalysts.[15] An alloy is a material formed by two or more metals (or metals and nonmetals) and can be classified as disordered or ordered. In disordered alloys, elements are randomly distributed within the crystal lattice, whereas in ordered alloys (also known as intermetallic compounds), elements are arranged according to specific patterns, exhibiting precise stoichiometric ratios and higher stability.[22, 23] Alloys not only leverage synergistic effects between multiple metals to achieve electronic restructuring,[24] but also modulate surface adsorption behavior through the coupling of different surface atoms, thereby altering reaction pathways and significantly enhancing electrochemical reaction kinetics.[25] Another notable advantage of alloys lies in their structural designability. By adjusting the compositions, crystal structures, particle sizes, defects, and interfaces of alloys, their electronic structures and catalytic reaction pathways can be effectively modulated.[26-29] Therefore, the formation of Ni-based alloys can significantly alter geometric and electronic structures, ultimately influencing their activity, selectivity, and stability during catalytic reactions.

Nevertheless, Ni-based alloy catalysts still face several challenges, including the further enhancement of intrinsic activity, the improvement of long-term stability under harsh oxidative and reductive conditions, the prevention of uncontrolled evolution of active species during electrochemical reconstruction, and the development of cost-effective and scalable synthesis methods. Therefore, systematically reviewing and summarizing the application of Ni-based alloys in electrocatalysis not only deepens our understanding of their structure-performance relationships but also provides crucial theoretical references and practical guidance for future catalyst design.

This review summarizes recent advances in Ni-based alloys for mainstream electrocatalytic reactions, encompassing synthesis methods, catalytic performance, device applications, and mechanisms. Despite that some review articles on Ni-based electrocatalysts have been published during the past years, most of them focus primarily on a broad range of Ni-based materials, especially compound materials (including oxides, hydroxides, sulfides, and heterogeneous materials),[30, 31] or on specific reactions (e.g., hydrogen evolution,[32] hydrogen oxidation,[33] and chemical oxidation[34-36]). The systematic review on the preparation and electrocatalytic applications of Ni-based alloys remain relatively scarce. In this review, we first review synthesis strategies for Ni-based alloys, including thermal treatment methods, liquid-phase-based synthesis methods, and vapor-phase methods. Subsequently, we summarize the latest progress of the developed advanced Ni-based alloys for applications in water electrolysis, fuel cells, metal-air batteries, and carbon dioxide reduction. Additionally, we discuss insights into the electrocatalytic mechanisms of Ni alloys and potential future directions for enhancing electrocatalyst performance. Through this review, we aim to provide readers with a unique perspective on the current state and future of this field.

2. Synthetic Methods of Ni-Based Alloy Catalysts

View Article Online
DOI: 10.1039/D5NR05514H

Selecting an appropriate synthetic method plays a crucial role in determining the microstructure, composition distribution, and ultimate catalytic performance of Ni-based solid solution and intermetallic compound electrocatalysts. To this end, this section systematically summarizes the main synthetic methods for Ni-based alloy electrocatalysts, focusing on analyzing the technical principles and research progress of thermal treatment methods, liquid-phase-based synthetic methods, and vapor-phase methods, while comparing the advantages and disadvantages of each approach. Finally, it outlines future development directions, aiming to provide valuable references for the research in this field.

2.1 Thermal Treatment Methods

The thermal treatment methods primarily rely on the interdiffusion of metal components at elevated temperatures to achieve alloying and ordering, serving as the main approach for preparing intermetallic compounds with ordered structures and high thermal stability.[37] These methods can be broadly categorized into two types: thermal melting and thermal annealing.

2.1.1 Thermal Melting. Thermal melting involves using extremely high temperatures (such as electric arc melting) to melt and uniformly blend metallic components, followed by rapid or controlled solidification to form an alloy. This method is suitable for synthesizing alloys with high-melting-point components and ensures product homogeneity and well-defined crystallographic phases. For instance, a series of Ni-Mo alloys, including NiMo, Ni_3Mo, Ni_4Mo, and Ni_6Mo, have been successfully synthesized by utilizing the extreme high temperatures generated by electric arcs for smelting (Fig. 1a).[38, 39] In a typical synthesis process, high-purity Ni and Mo were placed in an arc furnace under argon gas protection at the target stoichiometric ratio, and multiple remelting cycles (typically 3-5 times) were commonly employed to eliminate segregation and thus enhance compositional uniformity. Similarly, rare-earth metal-Ni intermetallics including $RENi_2$ (RE = Pr, Tb, Er)[40] and $LaNi_5$[41, 42] were also fabricated through this route, where the raw metals were arc-melted, often with multiple re-melting cycles, to yield homogeneous alloys. It was revealed that the composition and pressure of the atmosphere during arc melting significantly influenced the crystallinity and morphology of the products. Specifically, arc melting in an Ar/H_2 mixture yielded $LaNi_5$ nanoparticles with particle sizes ranging from 10 to 30 nm (Fig. 1b-c), exhibiting a significantly enhanced specific surface area (38.7 m^2 g^{-1}), far superior to that of bulk materials.[41] Furthermore, subsequent H_2 cycling treatment (repeated H_2 absorption and desorption) could further induce lattice distortion, grain refinement (average grain size reduced from 134 to 85 nm), and surface crack formation (Fig. 1d-j).[42] This significantly increased the electrochemically active surface area and optimized charge transport behavior. Additionally, the thermal melting method can be combined with dealloying strategies to achieve the controlled preparation of Ni-based intermetallic compounds with hierarchical porous structures (e.g., Co_3W-WNi_4 (Fig. 1k),[43] and $Mo(NiFeCo)_4$ [44]). This method

View Article Online
DOI: 10.1039/D5NR05514H

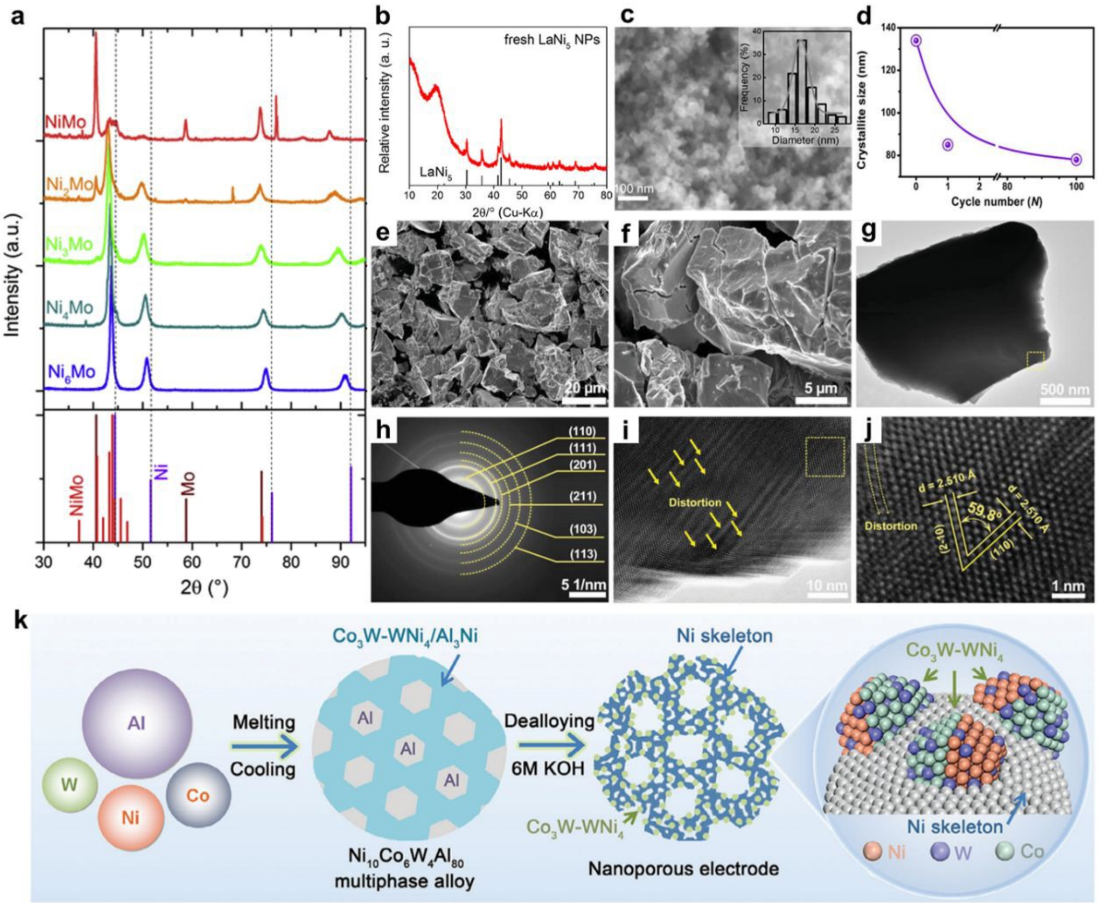

Fig. 1. Preparation of Ni-based alloys by thermal melting. (a) X-ray diffraction (XRD) patterns of the Ni-Mo alloys. Reproduced from ref.[38] with permission from Royal Society of Chemistry, copyright 2018. (b) XRD pattern, (c) scanning electron microscopy (SEM) image, and the particle size distribution (inset) of $LaNi_5$ nanoparticles. Reproduced from ref.[41] with permission from American Chemical Society, copyright 2020. (d) Dependence of crystallite size, (e, f) SEM images, (g) transmission electron microscopy (TEM) image, (h) corresponding selected area electron diffraction (SAED) pattern, and (i, j) high-resolution TEM (HRTEM) images of $LaNi_5$ after H_2 absorption-desorption cycle. Reproduced from ref.[42] with permission from Wiley-VCH, copyright 2023. (k) Schematic illustration for fabrication of hierarchical nanoporous Co_3W-WNi_4/Ni electrode. Reproduced from ref.[43] with permission from Wiley-VCH, copyright 2024.

first employed arc melting or vacuum melting techniques to melt Ni, Al, and target metals (e.g., Co, W, Mo, and Fe) at designed atomic ratios under high-purity inert atmospheres, producing uniform precursor alloys (e.g., $Ni_{10}Co_6W_4Al_{80}$, and $Ni_{12}Fe_2Co_2Mo_4Al_{80}$). Subsequently, the alloy was rapidly solidified into thin ribbons via melt spinning. A final chemical dealloying in alkaline solutions selectively etched Al elements, yielding continuous nanoporous skeletons with in situ anchored intermetallic nanoparticles. This method enabled seamless integration of active phases with conductive Ni frameworks, facilitating electron transfer and mass transport while enhancing structural stability.

2.1.2 Thermal Annealing. Thermal annealing is a critical post-processing step for regulating the crystallinity, composition distribution, and microstructure of Ni-based alloy catalysts. By precisely controlling annealing temperature, atmosphere, and duration, structural transformation from precursors to target alloy phases can be achieved. Typically, determining the appropriate annealing temperature is crucial for synthesizing catalysts with high specific surface area to expose more active sites, as excessively high temperatures often lead to grain overgrowth and coarsening.[45] This results in structural degradation of the catalyst, ultimately reducing its specific surface area. Conversely, excessively low temperatures may prevent precursors from fully reduction into an alloy with adequate conductivity, resulting in diminished catalytic performance.[46] Moreover, to further enhance product uniformity, particle size distribution control, and phase purity, thermal annealing is typically combined with other methods, such as hydrothermal-thermal annealing and coprecipitation-thermal annealing.

For instance, Jin et al. conducted a hydrothermal reaction at 150 °C for 20 h with ammonium molybdate as the Mo source to grow a Mo-Ni precursor network composed of ultrathin

View Article Online
DOI: 10.1039/D5NR05514H

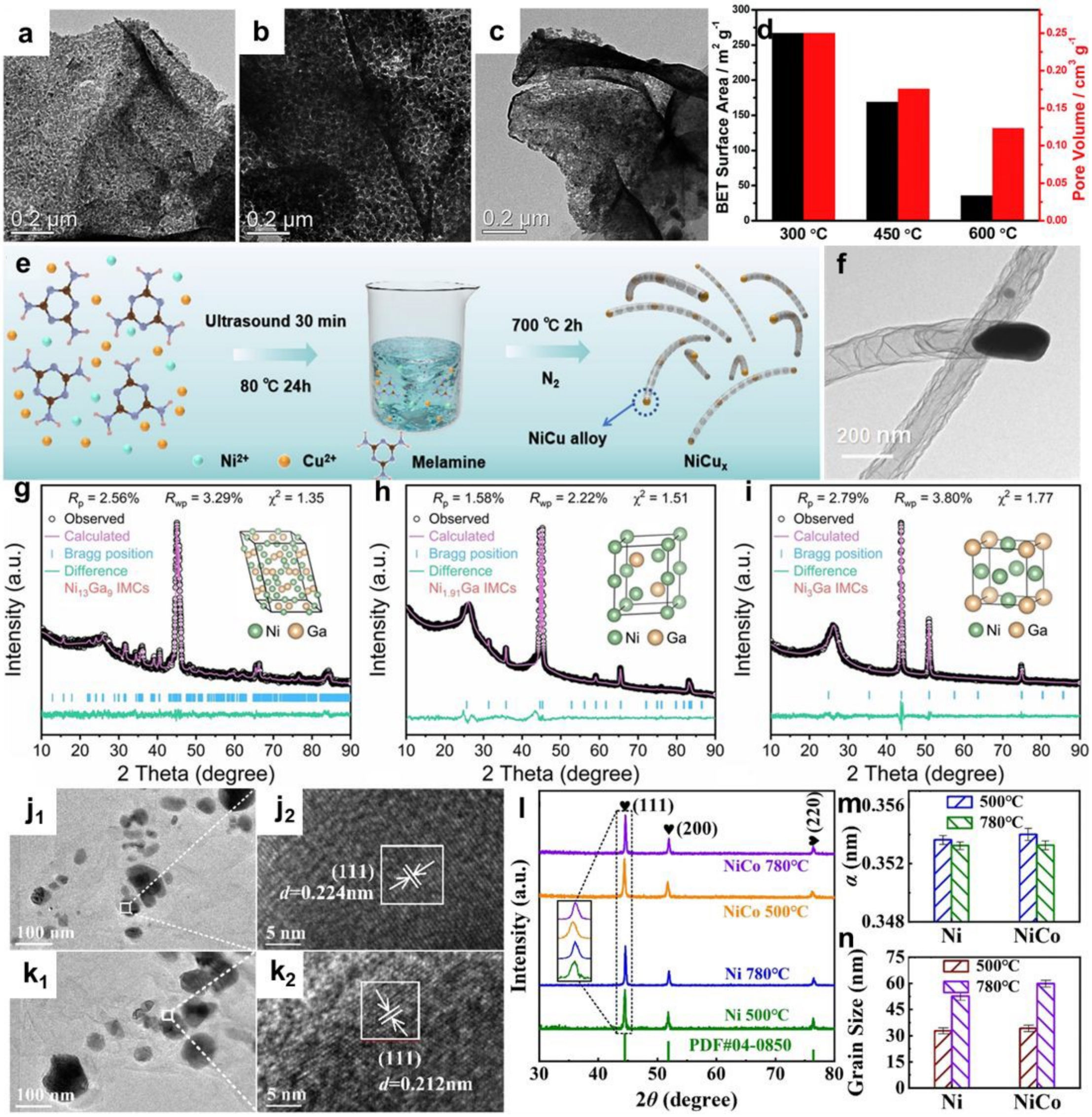

Fig. 2. Preparation of Ni-based alloys by thermal annealing. (a-c) TEM images, (d) Brunauer-Emmett-Teller (BET) surface area and the pore volume of porous $MoNi_4$ networks annealed at 300, 450 and 600 °C, respectively. Reproduced from ref.[46] with permission from Royal Society of Chemistry, copyright 2017. (e) Schematic illustration of the synthesis procedure, and (f) TEM images of NiCu alloy nanoparticles encapsulated within NCNTs. Reproduced from ref.[47] with permission from Elsevier, copyright 2025. (g-i) Rietveld refinement of XRD patterns for monoclinic $Ni_{13}Ga_9$ (g), hexagonal $Ni_{1.91}Ga$ (h), and cubic Ni_3Ga (i) intermetallic compounds. Reproduced from ref.[48] with permission from Wiley-VCH, copyright 2024. (j, k) TEM images of NiCo alloys prepared at different temperatures: NiCo-500 °C (j), and NiCo-780 °C (k). (l) XRD patterns, (m) lattice parameters, and (n) grain sizes of NiCo alloys. Reproduced from ref.[49] with permission from Royal Society of Chemistry, copyright 2024.

nanosheets on the surface of Ni foam. Subsequently, annealing at different temperatures (300, 450, and 600 °C) under H_2 atmosphere was performed to transform the precursor into crystalline $MoNi_4$ alloy. The annealing temperature affected the morphology, crystallinity, and porous structure of the final material. Annealing at 450 °C fully reduced the Mo-Ni precursor into $MoNi_4$ alloy while preserving its three-dimensional porous nanosheet network structure.[46] This maintained a high specific surface area (169.0 m^2 g^{-1}) and abundant mesoporous/macroporous channels. Below 300 °C, reduction was incomplete, while temperatures above 600 °C caused excessive grain growth and pore collapse, significantly reducing the specific surface area to 35.6 m^2 g^{-1} (Fig. 2a-d). This hydrothermal-thermal annealing two-step process provided an effective approach for precisely controlling the microstructure and crystallization behavior of Ni-based alloys. Zhang et al. synthesized a series of Ni-Mo intermetallic compounds supported on MoO_2 at different annealing temperatures. They first grew Ni-Mo-O precursors (such as $NiMoO_4$ nanocubes or hydroxides) on conductive substrates like Ni foam via hydrothermal synthesis, followed by programmed annealing in a reducing atmosphere (e.g., H_2/Ar mixture).[50] During annealing, the precursors underwent thermal reduction and structural rearrangement. By controlling the outward diffusion of Ni atoms and the reduction kinetics of Mo species, intermetallic nanostructures were in situ constructed. It should be noted that annealing temperature and duration decisively influenced the phase composition and morphology of the final product. At an annealing temperature of 500 °C, the $NiMoO_4$ precursor transformed into $MoNi_4$ nanoparticles anchored on a MoO_2 carrier. Increasing the annealing temperature to 600 °C further reduced the precursor to $MoNi_3$. Prolonging the annealing time promoted grain coarsening and enhanced crystallinity. Furthermore, the H_2 content in the reducing atmosphere influenced the reduction degree of metal oxides, thereby regulating alloy composition and surface chemical states.

The coprecipitation-thermal annealing method is also an efficient strategy for preparing Ni-based alloy catalysts with controllable structures. This approach typically employs layered double hydroxides as precursors, achieving uniform mixing of metal ions at the atomic scale through coprecipitation. Subsequent thermal treatment in a reducing atmosphere induces ordered atomic arrangement to form intermetallic phases. For instance, systems such as Ni-Ga,[51] Ni-Sn,[52] and Ni-In[53] have been successfully synthesized via this pathway. During the coprecipitation stage, controlling pH, precipitant type, and metal salt ratios directly influences the precursor's layered structure and metal distribution uniformity, thereby affecting the compositional homogeneity of the final alloy. During thermal annealing, temperature, duration, and atmosphere (e.g., H_2/Ar mixtures) are critical parameters determining alloy crystallinity, phase purity, and grain size. Higher annealing temperatures (typically 500-700 °C) promote atomic diffusion and ordering, forming distinct intermetallic structures, but excessively high temperatures may cause grain sintering and reduce specific surface area. Furthermore, hydrogen concentration in the reducing atmosphere influences the extent and rate of metal ion reduction, thereby regulating the alloy's surface structure and metal valence state. Csernica et al. achieved uniform mixing of Ni and Mo elements at the atomic scale via ammonia co-precipitation, forming a $NH_4HNi_2(OH)_2(MoO_4)_2$ precursor, which was subsequently thermally reduced under controlled atmospheres (5% H_2/95% Ar or N_2).[54] It was found that the Ni/Mo ratio in the precursor and the thermal reduction temperature were key parameters determining the final phase composition and morphology. Reducing a precursor with a Ni/Mo ratio of 1:1 at 1050 °C yielded a phase-pure, ordered Mo_7Ni_7 intermetallic compound with a dense structure and low surface roughness, primarily attributed to significant solid-state migration and sintering effects at high temperatures. In contrast, the $Ni_{0.92}Mo_{0.08}$ alloy synthesized with a Ni/Mo ratio of 9:1 and reduced at 550 °C retained a high specific surface area and submicron-scale pore structure, facilitating the exposure of more active sites. Thus, by precisely controlling parameters in the co-precipitation and thermal annealing steps, systematic structural design, from nanoparticle morphology and crystal plane exposure to atomic coordination environments, can be achieved, providing a reliable pathway for the targeted synthesis of high-performance Ni-based alloy catalysts.

To prevent agglomeration and sintering of alloy particles formed during high-temperature annealing, researchers developed a support-assisted thermal annealing strategy by impregnating metal precursors onto a substrate for calcination.[55, 56] For instance, Chen et al. prepared NiCo alloy/carbon composites derived from zeolitic imidazolate frameworks (ZIFs).[57] During pyrolysis of the precursor at 600 °C, carbon frameworks formed while uniformly distributed metal nodes underwent in situ reduction and confinement within the pores of carbon matrix, yielding uniformly distributed NiCo alloy nanoparticles with an average size of only 8.8 ± 1.9 nm. The abundant nitrogen-doped sites on the carbon substrate serve as anchoring points, stabilizing the metal particles through strong metal-support interactions. Moreover, its inherent micro-/mesoporous structure provided spatial confinement for alloy particle growth. Comparative experiments demonstrated that when pyrolysis temperatures increased to 700 and 800 °C, although carbon graphitization improved, the confinement capability of the carbon framework weakened. This led to significant agglomeration of NiCo nanoparticles, with average sizes increasing to 13.0 and 24.3 nm, respectively, accompanied by a decrease in specific surface area. Similarly, NiCu alloy nanoparticles encapsulated within nitrogen-doped carbon nanotubes (NCNTs) were synthesized via a straightforward impregnation-thermal annealing approach (Fig. 2e and f).[47] The procedure began with the homogeneous mixing of Ni^{2+} and Cu^{2+} precursors with melamine, followed by ultrasonication and drying. The resulting composite was subsequently annealed at 700 °C for 2 h under a nitrogen atmosphere. This thermal treatment facilitated the decomposition of melamine, while the concurrently formed NiCu alloy nanoparticles acted as catalytic templates guiding the growth of NCNTs. The NiCu alloy particles, with a controlled size of 5-10 nm, were uniformly distributed within the tubular carbon skeleton, demonstrating the significant confinement and anti-sintering effect of the nitrogen-doped carbon substrate on the metal particles during high-temperature processing. Zhang et al. prepared a series of Ni-Ga intermetallic compounds supported on nitrogen-doped reduced graphene oxide substrates by impregnating and mixing metal nitrate precursors with graphene oxide, followed by annealing under an H_2/Ar atmosphere. These compounds included monoclinic $Ni_{13}Ga_9$, hexagonal $Ni_{1.91}Ga$, and cubic Ni_3Ga (Fig. 2g-i).[48] The high specific surface area and abundant surface functional groups of the nitrogen-doped reduced graphene oxide effectively anchored the metal precursors, suppressing excessive migration of metal atoms and particle agglomeration during high-temperature annealing. This resulted in uniformly sized, well-dispersed Ni-Ga intermetallic compound nanoparticles without significant phase segregation or clustering.

Additionally, porous silica is frequently employed as a substrate for intermetallic compound growth. Its confinement effect, excellent thermal conductivity, and chemical stability facilitate rapid and uniform heating during high-temperature reduction processes, thereby minimizing sintering caused by localized overheating. For instance, nickel and zinc nitrate precursors were co-impregnated onto silica supports, followed by thermal reduction under a controlled H_2/Ar atmosphere to form well-dispersed Ni_3Zn intermetallic compounds.[58] This method allowed precise control over metal loading and facilitated the formation of charge-separated $Ni^{\delta-}$-$Zn^{\delta+}$ paired sites, which were critical for forming particles at the ultrafine nanoscale. Similarly, pore-filling co-impregnation has been applied to synthesize high-entropy intermetallic compounds such as NiFeCuGaGe supported on SiO_2. By drying mixed metal nitrate solutions under vacuum and the sequent high-temperature reduction at elevated temperatures, this approach enabled the formation of multi-element alloys with uniform elemental distribution and enhanced catalytic performance.[59] These cases demonstrate that a well-designed porous support can effectively provide physical isolation and electronic anchoring for high-surface-energy alloy nanoparticles during thermal annealing. This approach maintains high dispersion while achieving a highly crystalline alloy phase, thereby delivering an abundant and stable active interface for subsequent catalytic reactions.

To suppress particle agglomeration and sintering during high-temperature processing, introducing an inert matrix as a space-confining medium is also an effective strategy. For example, a NaCl matrix-assisted pyrolysis approach has been effectively employed to synthesize complex quinary NiCoFeMoZn catalysts.[60] This method involved homogenously dispersing metal precursors (e.g., acetylacetonates) in a aqueous solution containing polyvinylpyrrolidone and NaCl, followed by freeze-drying and subsequent calcination under a reducing atmosphere to achieve atomic-scale dispersion of metallic alloy within the NaCl matrix. The NaCl matrix, acted as a spatial confinement medium, not only mitigated nanoparticle agglomeration and promoted the formation of uniformly distributed alloys, but also facilitated the development of a three-dimensional macroporous carbon sponge structure. This enhanced electrolyte permeability and exposed a large amount of electroactive interface. Wu et al. synthesized $L1_0$-NiCo nanoparticles via an NaCl-mediated synthesis method using finely ground NaCl powders.[49] Metal precursors, such as nickel and cobalt acetylacetonates, were first dissolved and then uniformly mixed with the NaCl matrix through slow drying before undergoing high-temperature calcination at 780 °C under a reducing atmosphere. The difference in thermal expansion coefficients between the nascent alloy nanoparticles and the NaCl matrix induced compressive stress during the cooling process, which can promote atomic diffusion and facilitate the formation of the desired ordered intermetallic $L1_0$-phase (Fig. 2j-n). The final catalyst was easily obtained by simply washing away the NaCl medium with water, yielding clean nanoparticle surfaces free from surfactant contamination.

2.1.3 Other Thermal Treatment Methods. In addition to the aforementioned thermal treatment strategies, several innovative methods have also been developed for the synthesis of Ni-based alloy catalysts. Zhou et al. successfully fabricated hierarchical heterostructured porous intermetallic compounds in the Ni-Co-Al system by combining spark plasma sintering (SPS), aging treatment, and electrochemical dealloying techniques.[61] The process began with the fabrication of macroporous alloys using SPS under an argon atmosphere, which preserved intrinsic porosity and facilitated mass transport. Subsequent aging at 600-700 °C induced discontinuous precipitation, forming a γ/γ' lamellar nanostructure. Selective electrochemical dealloying of the γ phase then yielded aligned γ' nanoplates with a hierarchical porous architecture, significantly increasing the electrochemical surface area and exposing abundant active sites. This method effectively integrated structural control with compositional precision to enable the realization of self-supported catalysts. Berg et al. demonstrated the synthesis of NiGa and AlNi intermetallics via a two-step thermal diffusion and SPS process.[62] Precursor metals were mixed in stoichiometric ratios and heated under an inert atmosphere to facilitate interdiffusion, followed by SPS to consolidate the powders into dense, polycrystalline electrodes. Kumar et al. reported a molten salt-assisted solid-state route for synthesizing NiSi and Ni_2Si nanocrystals using Na_4Si_4 and $NiCl_2$ as precursors in a LiI-KI eutectic mixture.[63] The molten salt medium enhanced atomic diffusion at moderate temperatures (300-500 °C), enabling phase-selective formation of high-purity nanocrystals free of surface organic ligands. These synthesis methods offer entirely new opportunities for controlling the morphology and properties of Ni-based alloys to achieve highly efficient electrocatalytic performance.

Beyond the methods described above, the approach of combining mechanochemical synthesis with subsequent heat treatment has also attracted widespread attention. This two-step method offers unique advantages, including a simple operating process, the elimination of solvents and surfactants, and the ability to overcome the challenges of alloy formation caused by differences in the melting points of various metals, thereby yielding uniform Ni-based alloy catalysts with clean surfaces. Lee et al. first used high-speed ball milling to achieve uniform distribution of Ni and Pd acetylacetonate precursors on graphene, followed by thermal decomposition in a N_2 atmosphere at 400 °C, yielding highly dispersed NiPd alloy nanoparticles.[64] Due to the faster nucleation during the thermal decomposition of Pd-rich precursors, the alloy composition and particle size can be precisely controlled by adjusting the Ni/Pd molar ratio in the precursor mixture. As the Pd content increased, the average particle size decreased (from 6.5 to 4.0 nm), while the lattice spacing increased (from 0.216 to 0.220 nm). Xu et al. prepared self-supporting porous NiMo alloys using a combination of mechanical alloying with microwave sintering.[65] The addition of Mg powder as a space-filler during ball milling enabled the formation of a high-porosity structure after sintering at 900°C. Furthermore, the phase composition can be easily controlled by adjusting the initial molar ratio of Ni/Mo. Compared to the alloys with Ni/Mo ratios of 9:1 and 3:7, the alloy with a Ni/Mo ratio of 3:2 uniquely contained a large amount of NiMo intermetallic compounds. However, this method still has some inherent limitations that warrant attention, such as long processing time, high energy consumption, broad particle size distribution, and contamination from space-filling agents or unreacted precursors.

2.2 Liquid-Phase-Based Synthetic Methods

Liquid-phase-based synthesis methods have become one of the most commonly used approaches for preparing Ni-based alloy electrocatalysts with well-defined sizes, shapes, compositions, and crystal structures. Compared to thermal treatment methods, the liquid-phase-based synthesis methods enable the preparation of solid solutions or intermetallic compounds at relatively low temperatures (< 300 °C), contributing to energy savings and cost control.[66, 67] Due to the limitation of solvent boiling point, controlling experimental conditions in liquid-phase synthesis, such as the application of high-pressure conditions, the addition of reducing agents and capping agents, as well as the application of electric fields, is crucial for decreasing the kinetic energy barrier for the synthesis of Ni-based alloys.

2.2.1 Hydrothermal/Solvothermal Method. Hydrothermal/solvothermal synthesis is a liquid-phase method conducted under sealed conditions at elevated temperature and pressure. It is particularly suitable for preparing Ni-based alloy catalysts with controllable size and morphology by adjusting key parameters such as reaction temperature, pH value, surfactant type and concentration, reaction time, and reducing agent dosage.[68] Due to the significant changes in the physicochemical properties of water and other solvents under reaction temperatures exceeding their boiling points or high-pressure conditions, the reaction activity is markedly enhanced. This provides a potential pathway for overcoming high energy barriers and achieving liquid-phase synthesis of Ni-based alloys at mild conditions. It has been reported that reaction temperature is a key factor influencing the grain size of alloys. For instance, in the hydrazine-assisted hydrothermal synthesis of Ni-Co-Cu alloy, raising the temperature from 150 to 180 °C significantly reduced the average grain size from approximately 248 nm to about 109 nm.[69] This reduction was attributed to high temperatures which could promote nucleation while inhibit grain growth. pH also significantly impacted morphology: under alkaline conditions (pH 10-12), higher OH^- concentrations enhanced the activity of hydrazine reductant, accelerating nucleation and yielding smaller, more uniformly sized spherical particles. The introduction of surfactants effectively regulated particle size

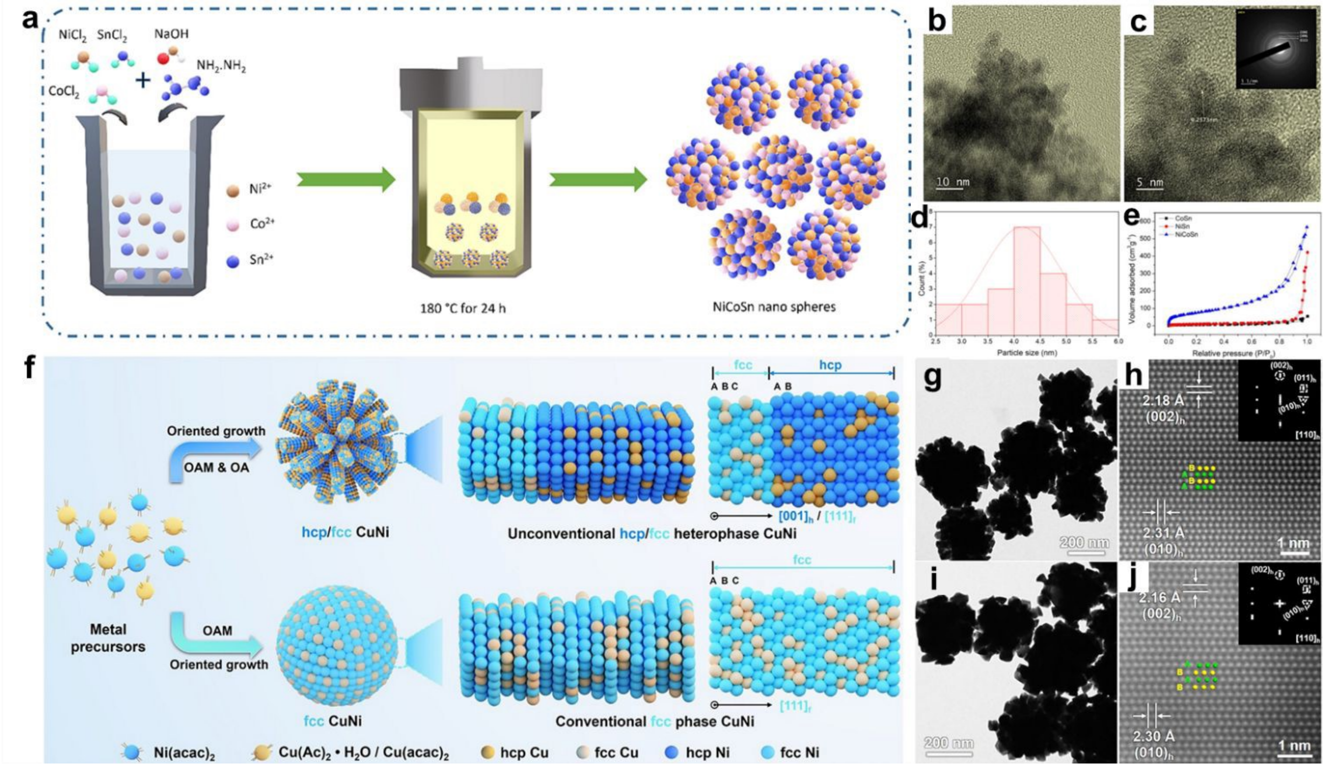

Fig. 3. Preparation of Ni-based alloys by hydrothermal/solvothermal method. (a) Schematic diagram of hydrothermal synthesis of NiCoSn alloys. (b, c) HRTEM images (inset shows corresponding SAED pattern), (d) particle size distribution, and (e) N_2 adsorption-desorption isotherm of NiCoSn alloys. Reproduced from ref.[70] with permission from Elsevier, copyright 2023. (f) Schematic illustration of the solvothermal synthesis of CuNi alloys with different phases. (g) TEM and (h) High-angle annular dark-field scanning transmission electron microscope (HAADF-STEM) images of hcp/fcc $Cu_{10}Ni_{90}$. Inset of (h): the corresponding fast Fourier transform (FFT) pattern. (i) TEM and (j) HAADF-STEM images of hcp/fcc $Cu_{30}Ni_{70}$. Inset of (j): the corresponding FFT pattern. Reproduced from ref.[71] with permission from Wiley-VCH, copyright 2025.

View Article Online
DOI: 10.1039/D5NR05514H

and dispersion. For instance, adding polyvinylpyrrolidone inhibited agglomeration by adsorbing onto particle surfaces, reducing the size of Ni-Co-Cu alloy particles from 248 to 154 nm while improving monodispersity. Reaction time influences crystal growth mechanisms and morphology evolution. As short reaction time favors the formation of fine primary nuclei, while a prolonged reaction allows particles to grow gradually through Oswald ripening and oriented aggregation, eventually tending toward sphericity. Sajeev et al. synthesized a NiCoSn alloy with an average diameter of approximately 4.2 nm using $NiCl_2·6H_2O$, $CoCl_2·6H_2O$, and $SnCl_2$ as metal precursors and hydrazine as a reducing agent in a strongly basic medium.[70] Compared to bimetallic counterparts (NiSn and CoSn) synthesized under similar conditions, the trimetallic NiCoSn alloy exhibited a significantly higher specific surface area (274 m^2 g^{-1}) and a mesoporous structure, attributed to the synergistic interaction among the three metals during hydrothermal growth (Fig. 3a-e). Additionally, surfactant and metal salt ratio are crucial factors in regulating the chemical composition and phase structure of alloy. In the Ni-Cu/reduced graphene oxide system, adjusting the Ni^{2+} to Cu^{2+} ratio to 4:1 achieved optimal nanoparticle dispersion and electrochemical active area.[72] In a typical mild hydrothermal synthesis of Ni-Cu nanoparticles, a mixture of nickel acetate and copper acetate precursors was reduced in an aqueous medium at a modest temperature of 95 °C for 4 h, utilizing a dual-surfactant system comprising sodium dodecyl sulfate and polyoxyethylene (10) isooctylphenyl ether (Triton X-100).[73] The use of surfactants not only stabilized the nanoparticles but also modulated their nucleation and growth kinetics, leading to spherical particles with uniform dispersion and an average size of 19-23 nm. The key to alloy formation was the Ni:Cu mass ratio, where a ratio of 2.0 facilitated the formation of a homogeneous Ni-Cu alloy phase, whereas a higher Ni content (Ni:Cu = 2.6) resulted in a bimetallic mixture without alloying, attributed to a depletion effect during co-reduction. The low-temperature hydrothermal conditions thus allow for precise control over alloying behavior and particle size, while avoiding excessive aggregation or oxidation.

In addition to the hydrothermal method, the solvothermal method has also been widely employed. Since solvents can serve as reducing agents, and their reducing abilities vary with changes in reaction temperature and pH, selecting an appropriate solvent is crucial for synthesizing alloy catalysts with the desired performance.[37] Wang et al. successfully synthesized CuNi nanoalloys featuring an unconventional hexagonal close-packed/face-centered cubic (hcp/fcc) heterostructure using a one-pot solvothermal strategy (Fig. 3f-j).[71] Using nickel acetylacetonate and copper acetate or copper acetylacetonate as metal precursors, the nucleation and growth of alloys were achieved through formaldehyde reduction in a mixed solvent system of oleylamine and oleic acid. Key synthesis parameters, particularly the initial atomic ratio of Cu to Ni, critically determined the crystal phase composition and nanostructure morphology of the final product. By precisely controlling precursor ratios, a series of hcp/fcc Cu-Ni alloys (hcp/fcc $Cu_{50}Ni_{50}$, $Cu_{30}Ni_{70}$, $Cu_{10}Ni_{90}$) were successfully synthesized. It was found that a higher Ni content promoted the formation and stabilization of the hcp phase. Concurrently, the synergistic effect of the oleylamine and oleic acid surfactants guided the oriented growth of the nanostructure, ultimately yielding nanoalloys with a multi-branched morphology. Time-dependent experiments further elucidated the morphology evolution mechanism: during the initial reaction phase, fcc-phase Cu-rich alloy nanoparticles formed. As the reaction proceeded, Ni^{2+} underwent continuous reduction, and the Cu-Ni alloy grew along the $[111]_{fcc}/[001]_{hcp}$ direction under the regulation of oleylamine and oleic acid, ultimately forming hcp/fcc heterophase branched nanostructures with Cu-rich cores and Ni-rich shells. By precisely controlling precursor chemistry and reaction kinetics, this synthesis method enabled effective regulation of crystal phases and nanostructures of non-precious metal alloy, providing a crucial synthetic foundation for designing high-performance electrocatalytsts.

2.2.2 Co-reduction Method. Co-reduction method has emerged as a key strategy for preparing Ni-based alloy nanomaterials with uniform composition and size, owing to its ability to achieve simultaneous reduction and nucleation of precursors in the liquid phase. By precisely controlling the ratio of metal precursors, the type of reducing agent, reaction temperature and duration, as well as the surfactant system, this method enables fine-tuned regulation of composition, crystal structure, and morphology of alloys.[74] For instance, Liu et al. successfully synthesized Ni_xM_y (M = Ga, Sn) intermetallic compound nanocrystals by employing a co-reduction strategy in oleylamine, using tert-butylaminoborane or n-butyllithium as reducing agents. At a reaction temperature of 220-250 °C, ordered intermetallic phases such as cubic, orthorhombic, or hexagonal Ni_3Ga and Ni_3Sn_2 with sizes ranging from 3.5 to 7.5 nm can be successfully prepared (Fig. 4a-c).[75] The selection of reductant was critical: the tert-butylaminoborane facilitated the formation of Ni-H species to aid Ga^{3+} reduction, while the n-butyllithium promoted metal-oleylamide formation for the synthesis of Ni_3Sn_2, ultimately yielding ordered intermetallic phases after thermal annealing. Li et al. synthesized NiSn nanoparticles with tunable stoichiometric ratios using $Ni(acac)_2$ and $Sn(oac)_2$ as metal precursors, and oleylamine, tri-n-octylphosphine, oleic acid, and borane tert-butylamine as solvents, stabilizers, surfactants, and reducing agents, respectively.[76] This method produced core-shell NiSn alloy nanoparticles with a size of approximately 4 nm (Fig. 4d-g). Their surfaces exhibited an amorphous structure, while the cores retained the structure of Ni_3Sn_2 intermetallic compound (Fig. 4h). Moreover, by removing oleic acid or tri-n-octylphosphine from the synthesis system, NiSn nanoparticles with Ni_3Sn_4 crystalline phases in the form of large spherical aggregates or chain-like aggregates were prepared, respectively. In the co-reduction synthesis of Cu/NiCu core-shell nanowires, the core-shell structure and one-dimensional morphology are integrated by first forming a Cu nanowire core at 185 °C, followed by depositing a NiCu alloy shell layer at 210-

View Article Online
DOI: 10.1039/D5NR05514H

230 °C. The shell thickness and alloy composition increased with rising temperature. It has been shown that oleylamine, oleic acid and tri-n-octylphosphine in the reaction system not only stabilized nanoparticles and prevented aggregation but also regulated

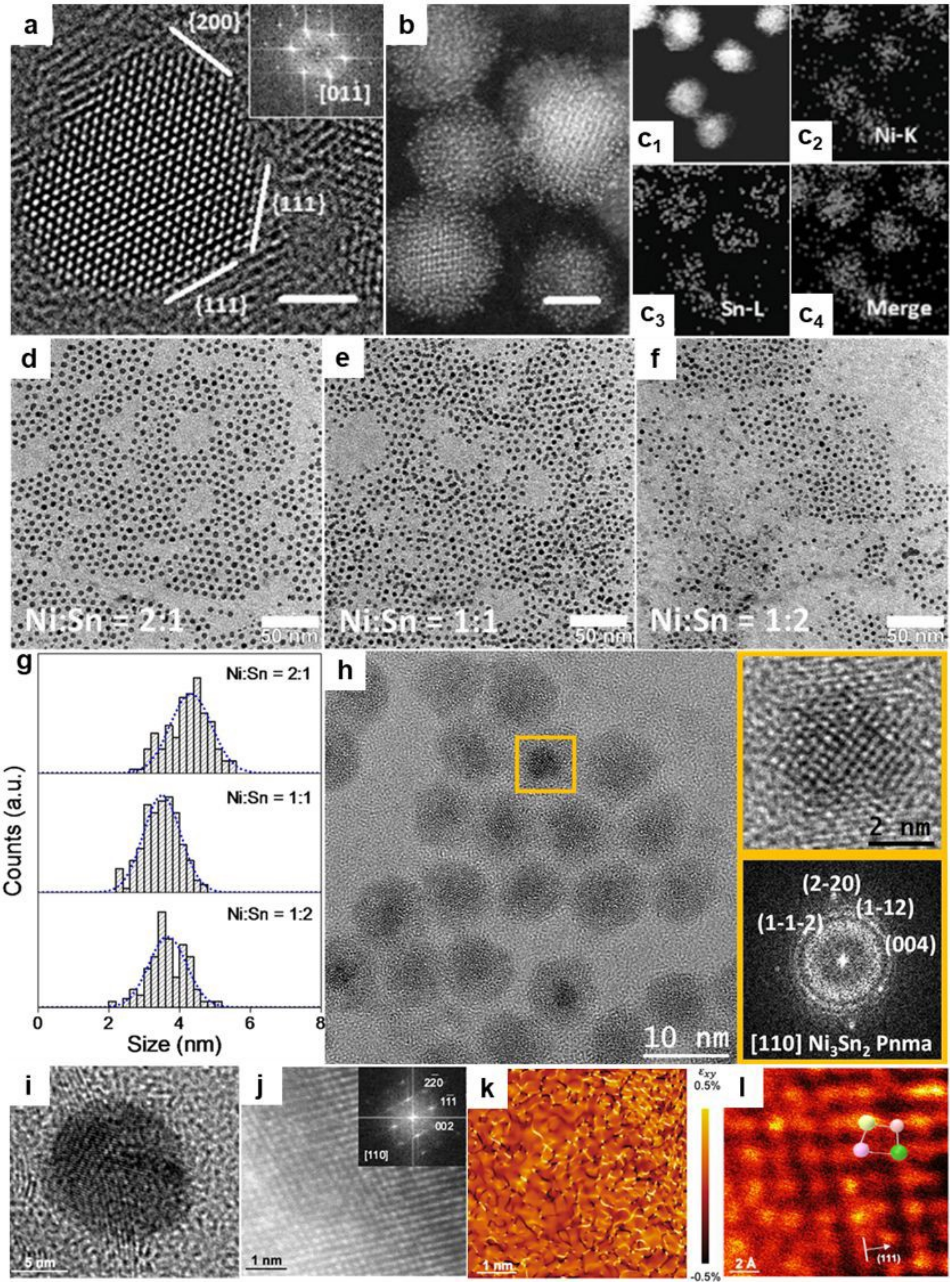

Fig. 4. Preparation of Ni-based alloys by co-reduction method. (a) Aberration-corrected TEM image of Ni_3Ga nanocrystals (the inset shows the FFT pattern). (b) Aberration-corrected STEM image and (c) STEM-energy dispersive X-ray spectroscopy (EDX) elemental mapping images of Ni_3Sn_2. Scale bars: 2 nm. Reproduced from ref.[75] with permission from Wiley-VCH, copyright 2016. (d-f) TEM images of NiSn nanoparticles with different nominal Ni:Sn ratios: 2:1 (d), 1:1 (e), and 1:2 (f), and the corresponding size distribution histograms (g). (h) HRTEM images and the corresponding FFT pattern of NiSn (2:1) nanoparticles. Reproduced from ref.[76] with permission from Elsevier, copyright 2018. (i) TEM image of a single $Fe_{12}Co_{28}Ni_{33}Mo_{17}Pd_5Pt_5$ alloy nanoparticle. (j) STEM image and

the corresponding FFT pattern (inset). (k) Strain map from geometric phase analysis. (l) Atomic-resolution STEM revealing lattice distortion. Reproduced from ref.[77] with permission from National Academy of Sciences, copyright 2025.

View Article Online
DOI: 10.1039/D5NR05514H

crystal facet growth through selective adsorption, thereby influencing the final product's morphology and phase purity.[78] Additionally, guided by AI, Kim et al. achieved the automated and controllable synthesis of multi-component alloy nanoparticles by precisely regulating the ratio of metal acetylacetonate precursors (including Mn, Fe, Co, Ni, Cu, Mo, Pd, and Pt) and $Mo(CO)_6$ through an automated liquid handling system.[77] Optimal co-reduction synthesis conditions were determined through experimental design: oleylamine solvent, no carbon nanotube additive, reaction temperature of 200 °C, reaction time of 12 h, and precursor concentration of 10 mM. These conditions were critical for achieving uniform particle size and elemental distribution, as lower temperatures (e.g., 120 °C) resulted in insufficient metal-ligand bond cleavage and phase separation. The presence of Pd was found to promote the formation of a fcc structure, acting as a nucleation seed that facilitated the incorporation of other metals. The resulting Ni-rich high-entropy alloy ($Fe_{12}Co_{28}Ni_{33}Mo_{17}Pd_5Pt_5$) exhibited a highly distorted lattice and uniform elemental dispersion (Fig. 4i-l). Therefore, by systematically optimizing precursor chemistry, reduction kinetics, and surface chemical environment, the co-reduction method provides an important pathway for the rational design of Ni-based alloy electrocatalysts with specific composition, structure, and morphology.

2.2.3 Electrochemical Deposition Method. In the controlled synthesis of Ni-based alloy electrocatalysts, electrodeposition has emerged as an effective method for preparing alloys with specific morphologies and compositions due to its operational simplicity, mild conditions, and scalability.[79-82] Precise control over electrodeposition parameters such as electrolyte composition and pH, as well as the applied potential or current density, enables fine-tuning of the alloy microstructure. As demonstrated by Alagesan et al., increasing the current density from 4 to 12 A dm^{-2} during the electrodeposition of Ni-Re alloys systematically reduced the Re content from 38 to 15 wt%.[83] Concurrently, the deposited layer morphology evolved from a matte surface to a granular and eventually cauliflower-like structure, significantly increasing the electrochemically active surface area. Further electrochemical activation introduced significant lattice strain (up to 7.2%), which originated from the insertion/extraction of K^+ ions in the alkaline electrolyte and was directly correlated with enhanced catalytic activity. In the alkaline lactic acid bath electrodeposition of Ni-W alloys, increasing the current density from 3.33 to 10 mA cm^{-2} elevated the W content from 6.35 to 16.17 wt%.[84] Concurrently, the deposited layer morphology transformed from dense particles to a nanostructure exhibiting wrinkled features, significantly enhancing the electrochemically active surface area. The lactate ions acted as ligands to promote the induced co-deposition of W, yielding nanoalloys with a W content as high as 35.8 wt%. To overcome issues like poor deposition uniformity caused by the side reaction of water electrolysis in aqueous systems, Liu et al. developed a deposition scheme based on aqueous deep eutectic solvents (DES).[85] It was revealed that the water content in DES (1-5 wt%) profoundly influenced the deposition process. An optimal water content (e.g., 3 wt%) promoted the formation of a moderate $Ni(OH)_2$ colloidal film over the substrate, guiding the growth of a uniform, dense Ni-Cu alloy deposition layer with an optimized Ni/Cu ratio (Fig. 5a-h). Conversely, excessively high or insufficient water content leaded to excessive $Ni(OH)_2$ precipitation or alloy particle agglomeration, respectively, compromising structural homogeneity. Similarly, Ni-Mo alloys were electrodeposited from DES baths composed of choline chloride and propylene glycol, with $NiCl_2·6H_2O$ and $(NH_4)_6Mo_7O_{24}·4H_2O$ as metal precursors and citric acid as a stabilizer. The deposition was carried out under constant potential conditions (-0.6 V vs. Ag quasi-reference) at 60 °C, resulting in nanocrystalline coatings with spherical morphologies and grain sizes of ~5-15 nm.[86] The surface exhibited a spherical-flat morphology accompanied by a network of microcracks, with a phase composition gradient distributed along the thickness direction. The surface was enriched with the $Mo_{0.20}Ni_{0.80}$ intermetallic compound. The introduction of citric acid into the plating bath further smoothed the coating surface and influenced Mo content (e.g., decreasing from 6.6 to 5.3 wt%), indicating that the complexing agent modulated elemental co-deposition behavior. Witten et al. adjusted the pH of an electrolyte containing $NiSO_4$, Na_2MoO_4, and sodium citrate to 9.2 using $NH_3·H_2O$, subsequently successfully preparing Ni-Mo alloys on Ti substrates via electrodeposition.[87] Citrate ions functioned as effective chelating agents, binding Ni^{2+} and MoO_4^{2-} ions to modulate their reduction potentials and promote co-deposition. Additionally, their buffering effect helped maintain pH stability in the electrolyte during deposition, thereby influencing deposition kinetics and alloy composition uniformity. Electrodeposition was conducted at a constant current of -100 mA for 1200 s, supplemented by stirring to ensure uniform mass transfer. The resulting Ni-Mo deposit exhibited a typical amorphous granular morphology with micrometer-scale cracks on the surface. This morphology was closely related to the release of internal stresses during electrodeposition and the crystallization behavior controlled by complexation-reduction kinetics. In the synthesis of P-CuNi alloys, adjusting the electrolyte to a weakly acidic environment using NH_4F effectively suppressed metal ion hydrolysis, guiding the formation of microsphere structures assembled from sub-nanometer flakes.[88] The electrodeposition mode and parameters critically influence the resulting alloy morphology and microstructure. For instance, Qin et al. successfully fabricated a dense, granular, and uniform high-entropy alloy CoNiCuMoZn coating using pulsed electrodeposition by regulating deposition parameters (e.g., 0.2 s on/0.8 s off at a current of 4 A).[89] Subsequent electrochemical restructuring via cyclic voltammetry in a controlled potential window can further

View Article Online
DOI: 10.1039/D5NR05514H

transform the surface into wrinkled spherical particles, enhancing active site exposure and introducing metal vacancies (e.g., Mo vacancies), which are crucial for catalytic performance. Alternatively, potentiostatic electrodeposition at a fixed negative potential (e.g., -2.0 V vs. Hg_2SO_4) can yield three-dimensional cauliflower-like architectures with dual-layer structures comprising crystalline surfaces and amorphous/crystalline mixed phases, as observed in FeCoNiZnP (Fig. 5i-j).[90]

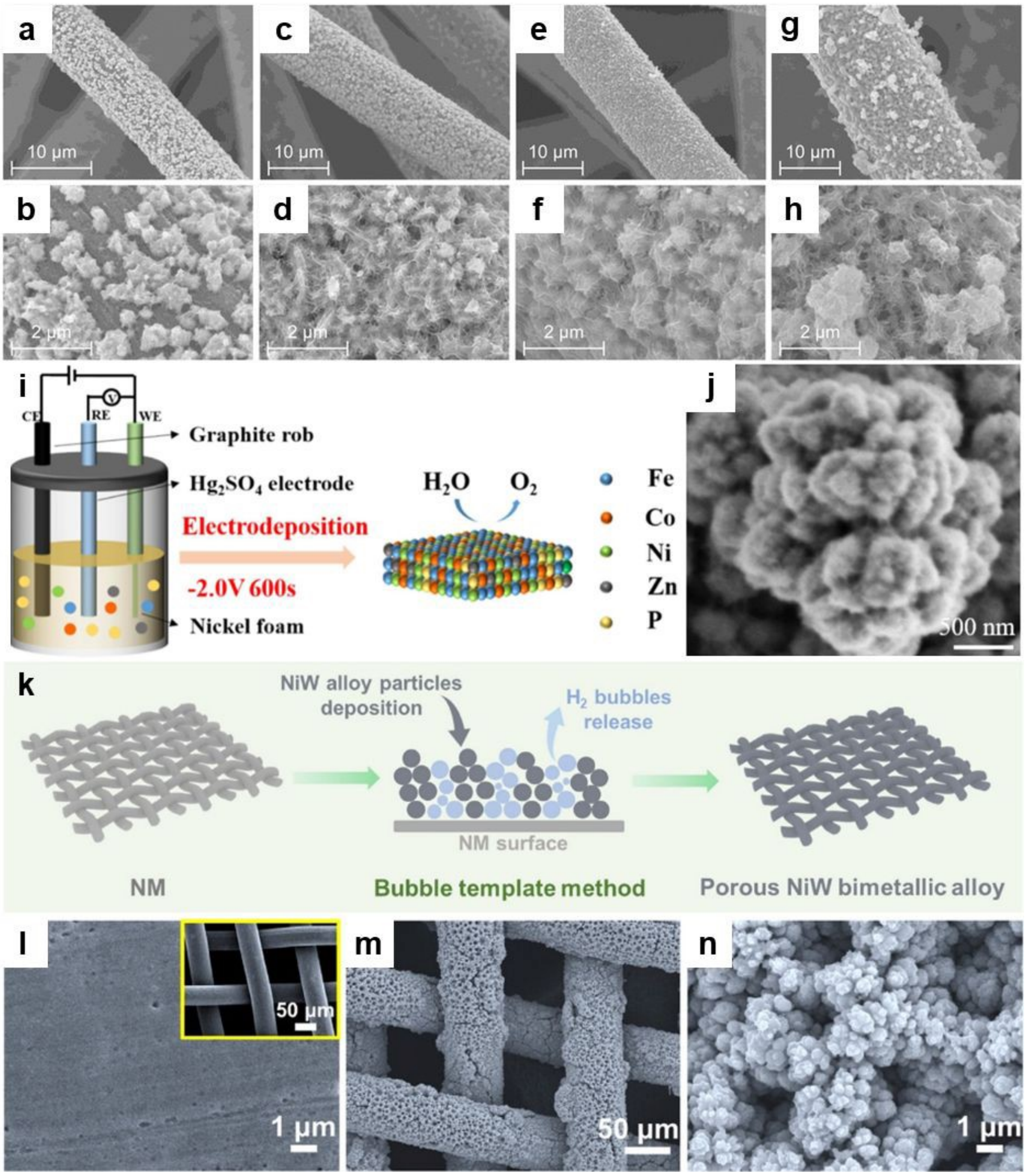

Fig. 5. (a-h) Preparation of Ni-based alloys by electrodeposition method. SEM images of the Ni-Cu alloys fabricated using DES-based solutions with water contents of 0 wt% (a, b), 1 wt% (c, d), 3 wt% (e, f), and 5 wt% (g, h). Reproduced from ref.[85] with permission from Royal Society of Chemistry, copyright 2025. (i) Schematic illustration for synthesis of FeCoNiZnP. (j) SEM image of cauliflower-like FeCoNiZnP surface. Reproduced from ref.[90] with permission from Elsevier, copyright 2025. (k) Schematic illustration of the synthetic process for the porous NiW alloy. (l-n) SEM images of the Ni mesh (l), and porous NiW alloy (m, n). Reproduced from ref.[91] with permission from Wiley-VCH, copyright 2025.

In addition, dynamic templating methods are widely employed to construct three-dimensional structures with high specific surface area and superior mass transfer properties. Li et al. employed H_2 bubbles generated in situ at high cathode

View Article Online
DOI: 10.1039/D5NR05154H

current densities as soft templates to guide the deposition of Ni-W alloy onto the substrate surface.[91] This process ultimately produced porous structures with interconnected channels and particle sizes of approximately 200-300 nm (Fig. 5k-n). This structure significantly increased the number of active sites while enhancing electrolyte permeation and bubble release. In summary, by regulating current density, electrolyte composition (e.g., DES and water content) and pH, and employing electrodeposition strategies such as dynamic templating, Ni-based alloys with diverse morphologies, ranging from dense films to three-dimensional porous frameworks, can be controllably fabricated. This approach establishes a robust material foundation for optimizing their catalytic performance.

Ultrasonic-assisted electrodeposition has attracted widespread attention in the preparation of high-performance Ni-based alloy catalysts due to its unique advantages in microstructural control and dispersion strengthening. This technique utilizes microjets and shock waves generated by the ultrasonic cavitation effect to effectively suppress nanoparticle agglomeration, enhance interfacial mass transfer, and significantly improve the density and grain refinement of the deposited layer.[92] Due to its flexible parameter control and broad applicability, this method has been widely used in the preparation of alloy electrodes such as NiCo,[93] NiCu,[94] NiZn,[95] NiMo,[96] and NiW,[97] as well as their composite materials for electrocatalytic reactions. For example, Li et al. successfully prepared Ni-Cu/TiN nanocomposite coatings in a sulfate-citrate system using an ultrasonic-assisted electrodeposition method, and systematically investigated the effects of ultrasound and current density on the morphology and structure of the coatings.[94] The results indicated that the introduction of ultrasound effectively promoted the uniform dispersion of TiN nanoparticles in the electroplating solution and significantly influenced the evolution of the surface morphology and texture of the coatings. When the current density was increased from 2 to 5 $A \cdot dm^{-2}$, the coating surface gradually transformed from loose, cauliflower-like particles to a dense, smooth cellular structure, with grain sizes refined to 14-22 nm. Concurrently, the preferred orientation was (200) plane and the relative texture coefficient reached a maximum of 57.04%, indicating that grain growth exhibited distinct preferential orientation. Upon further increasing the current density to 6 $A \cdot dm^{-2}$, the grains coarsened slightly, and the content of TiN particle decreased, indicating the existence of an optimal current density range for structural optimization. In addition, ultrasonic-assisted deposition resulted in an average surface roughness (R_a) of 26-34 nm for the Ni-Cu/TiN coating, a significant increase compared to the Ni-Cu alloy deposited without ultrasonic assistance (R_a = 4-5 nm), which is beneficial for increasing the electrochemical active area. Nevertheless, ultrasonic-assisted electrodeposition still faces certain limitations in the synthesis of Ni-based alloys. First, there is a complex nonlinear coupling relationship between ultrasonic parameters and electrodeposition conditions, and there is currently a lack of systematic parameter optimization strategies and universal control models. Second, excessively high ultrasonic intensity may cause localized cavitation damage on the electrode surface, compromising the interfacial bonding between the coating and the substrate and affecting the long-term stability of the electrode.

2.2.4 Microwave-Assisted Liquid-Phase Synthesis. Microwave-assisted liquid-phase synthesis has emerged as a promising approach in the preparation of Ni-based alloys due to its unique heating mechanism. This method utilizes the coupling effect between microwaves and polar solvents or metal precursors to achieve rapid and uniform bulk heating, thereby overcoming issues such as large temperature gradients and slow reaction kinetics associated with traditional oil-bath heating. This highly efficient dielectric heating method not only reduces reaction time from several hours to just a few minutes but also enables kinetic control over the nucleation and growth processes of the alloys through precise regulation of process parameters, thereby yielding nanocrystals with high purity, narrow particle size distributions, and specific morphologies.[98] Based on these advantages, microwave-assisted liquid-phase synthesis has been successfully applied to the preparation of electrocatalysts for various Ni-based alloys and intermetallic compounds, including NiBi,[99, 100] NiSb,[100] NiSn,[100] NiCoCr,[101] and NiCu.[102] For instance, Teichert et al. reported the synthesis of a series of Ni−M (M=Sn, Sb, Bi) intermetallic compounds via a microwave-assisted polyol method.[100] The study demonstrated that the phase purity and product crystallinity could be effectively controlled by adjusting the reaction temperature (240-300 °C), the precursor ratio, and the addition of surfactants such as KOH or oleylamine. In the Ni-Sn system, by precisely controlling the Ni/Sn precursor ratio and reaction temperature, a pure-phase β-Ni_3Bi_2 was successfully obtained, exhibiting a rose-like aggregate morphology. In contrast, in the Ni-Sb system, phase control from the Ni-rich α-Ni_3Sb to NiSb can be achieved by simply altering the Ni/Sb feed ratio. Besides, the addition of KOH was crucial for obtaining pure-phase Ni_5Sb_2. Dong et al. utilized a one-step microwave method to synthesize NiCoCr alloy with a three-dimensional porous network structure in situ on Ni foam.[101] They found that microwave power (800-1000 W) and irradiation time (150-210 s) directly influenced the nucleation density and growth rate of alloys. Treatment at 1000 W for 180 s yielded the optimal structure with uniform morphology and abundant pores, whereas too short a time leaded to incomplete reaction, and too long a time caused the network structure to stack and agglomerate, thereby reducing the electrochemical active surface area. However, the microwave-assisted liquid-phase synthesis also has certain limitations. First, the products of this method are often highly sensitive to reaction parameters, even slight fluctuations in temperature or precursor concentration can lead to the formation of impurity phases. Second, the universality of this method is constrained by the boiling point and reducing capacity of the solvent.

2.3 Vapor-phase Methods

The vapor-phase method offers significant advantages in preparing Ni-based alloy electrocatalysts, particularly enabling atomic-level precision in the preparation of thin films or low-dimensional materials. This approach typically involves converting precursors into the gas phase, followed by chemical reactions or physical deposition to form the target material on the substrate surface.[103]

View Article Online
DOI: 10.1039/D5NR05514J

2.3.1 Chemical Vapor Deposition (CVD). CVD is a method for depositing thin films through chemical reactions between gaseous precursors and heated substrate surfaces. As a film/coating preparation technique offering high purity, high uniformity, and material diversity, CVD demonstrates unique advantages in preparing Ni-based alloy catalysts supported on two-dimensional materials.[104-107] By controlling parameters such as deposition temperature, deposition time, and metal precursor ratio, the morphology and size of thin-film alloys can be precisely regulated, thereby significantly influencing their catalytic performance. For instance, Babar et al. employed aerosol-assisted CVD to fabricate NiPd nanoalloy films with varying thicknesses at 475 °C by controlling the deposition time (Fig. 6a-d).[108] As the deposition time extended from 60 to 120 min, nanoparticles aggregated to form spherical bead-like structures, with particle size gradually increasing and surface roughness rising. Further prolonging the time to 180 min resulted in a pronounced sintering effect, where particles fused to form a dense film layer. Consequently, the original nanostructure gradually disappeared, and the surface became increasingly smooth, leading to a decline in electrocatalytic performance. A Scotch tape test confirmed that all samples

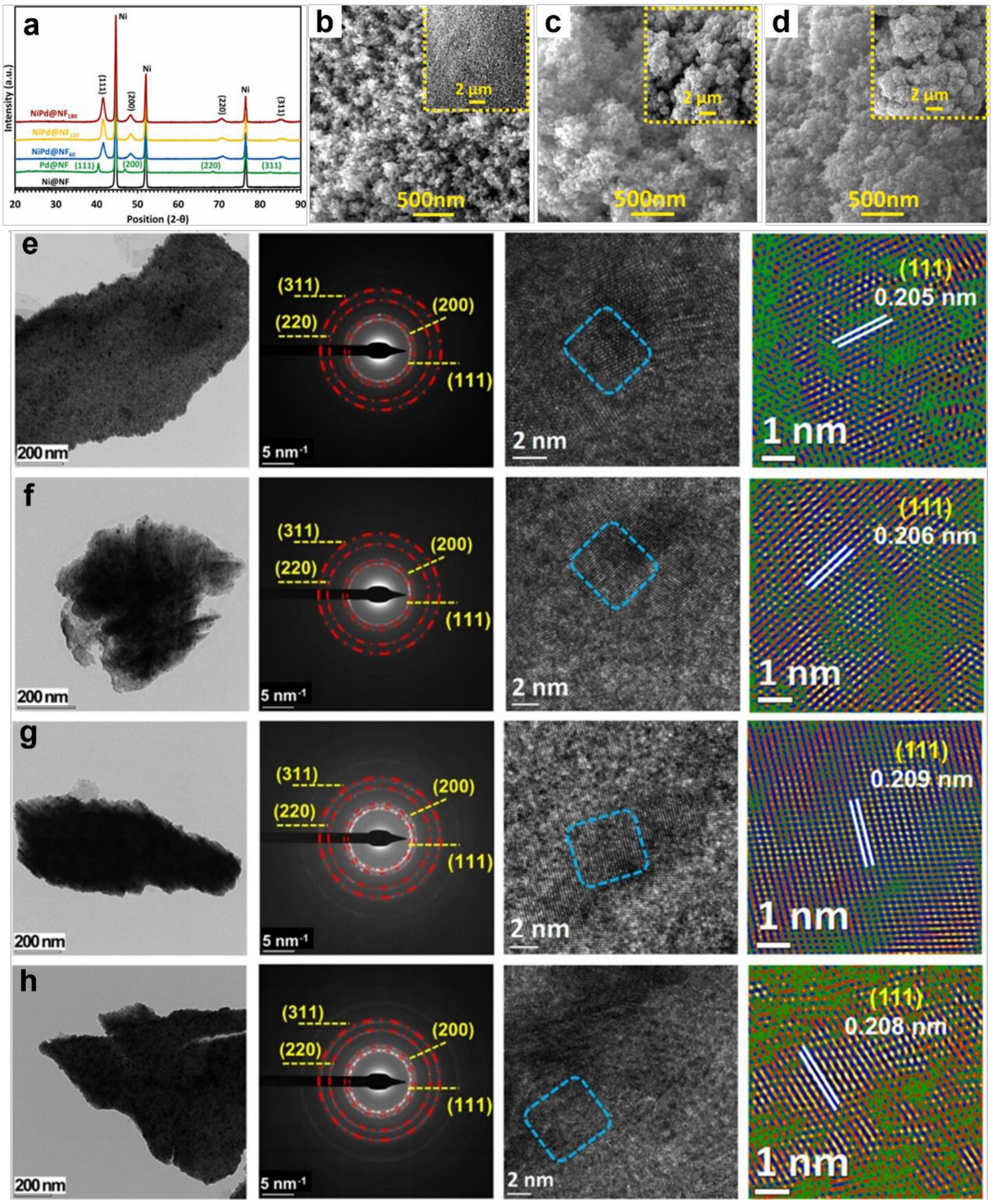

View Article Online
DOI: 10.1039/D5NR05514H

Fig. 6. Preparation of Ni-based alloys by vapor-phase method. (a) XRD patterns, (b-d) SEM images of NiPd alloys fabricated at different deposition times of 60 (b, NiPd@NF$_{60}$), 120 (c, NiPd@NF$_{120}$) and 180 (d, NiPd@NF$_{180}$) min. Reproduced from ref.[108] with permission from Elsevier, copyright 2022. (e-h) TEM images, SAED patterns, HRTEM images, and corresponding interplanar spacing measurements associated with the {111} planes of FeCoNiCu (e), FeCoNiCuV (f), FeCoNiCuMo (g), and FeCoNiCuW films (h). Reproduced from ref.[109] with permission from American Chemical Society, copyright 2025.

exhibited adhesion retention values exceeding 98%. Furthermore, long-term electrochemical testing revealed no decrease in activity or deterioration in morphological features for the prepared films, indicating that CVD possessed significant advantages in fabricating highly stable Ni-based alloy thin films. Komatsu et al. synthesized a series of Ni_3Ge intermetallic compounds within mesoporous silica MCM-41 by controlling CVD parameters such as deposition temperature, duration, and precursor flow rate.[107] These parameters critically influenced the stoichiometry, particle size, and dispersion of the resulting intermetallic compounds. Under optimal conditions, a near-stoichiometric Ni/Ge atomic ratio (approximately 3.0) was achieved, corresponding to minimal metal oxide formation within the resulting Ni_3Ge phase. The confinement effect imparted by the mesoporous carrier further suppressed particle growth, yielding uniformly sized Ni_3Ge nanoparticles (2-3 nm) within the pore channels. The incorporation of Ge endowed Ni_3Ge with unique geometric and electronic effects, resulting in higher catalytic activity than pure Ni. This approach demonstrates that precisely controlling CVD parameters in combination with a customized porous carrier enables the directed synthesis of well-defined nanoscale intermetallic compounds with enhanced structural uniformity.

2.3.2 Physical Vapor Deposition (PVD). PVD converts source materials into a gaseous state through physical methods such as evaporation or sputtering, then deposits them onto a substrate surface to form thin films.[110, 111] Compared to CVD, PVD generally does not involve complex chemical reactions, making them more suitable for preparing high-purity thin films with precisely controlled compositions. Among these, arc plasma evaporation has emerged as an effective method for preparing Ni-based intermetallic compound nanoparticles with long-range ordered crystal structures due to its extremely non-equilibrium process characteristics, which employs Ni-based alloys (e.g., Ni-Al, Ni-Sn, and Ni-Fe-Mg) as cathode targets.[112-115] Within an inert atmosphere, a high-energy arc generates an ultra-high-temperature plasma (> 10,000 K), causing the raw material to vaporize instantaneously. Subsequently, the metal vapor undergoes ultra-rapid condensation under high-pressure inert gas, a process that significantly suppresses compositional segregation and promotes the direct formation of thermodynamically metastable or highly ordered intermetallic phases (e.g., $L1_2$-Ni_3Al, and Ni_3Sn). By controlling the initial stoichiometry of the target material, arc power, and chamber pressure, the phase composition and particle size distribution of the products can be precisely regulated at the nanoscale. For example, Xu et al. successfully used this method to prepare nanoparticles dominated by ordered Ni_3Al with a small amount of Ni-rich solid solution.[112, 113] During a controlled passivation process, a thin oxide layer formed on their surfaces, creating a core-shell structure. Crucially, the spontaneously formed aluminum oxide nanofiber network within this process served as a structural support to effectively disperse and anchor active intermetallic compound nanoparticles, creating an inherently anti-agglomerative, high-surface-area multiphase composite architecture. Garstenauer et al. evaporated pure Te under static conditions, followed by depositing it onto a Ni/C catalyst through precise temperature control, and successfully prepared a series of carbon-supported nickel telluride intermetallics (Ni-Te/C) with varying Ni:Te atomic ratios.[116]

Magnetron sputtering stands as one of the most widely used PVD techniques that utilizes the combined effects of magnetic and electric fields to control the sputtering process. During magnetron sputtering, gas ions (such as argon ions) are accelerated by the electric field and collide with the target surface, causing atoms from the target to be sputtered off. These sputtered atoms then deposit onto the substrate, forming a thin film. The introduction of a magnetic field enhances sputtering efficiency while improving film uniformity and adhesion.[117, 118] By adjusting parameters such as target composition, sputtering power, temperature, and gas pressure, the compositions and distribution of alloying elements can be precisely modulated, enabling the controlled synthesis of multi-component alloys or high-entropy alloys. Guided by the density functional-theory (DFT) calculation, Wang et al. employed magnetron sputtering technology to fabricate a series of single-phase fcc high-entropy alloys with well-defined crystal structures by controlling sputtering parameters such as pressure, power, and target-substrate distance. These dense alloys exhibited uniform elemental distribution without phase separation or segregation (Fig. 6e-h).[109]

The vapor deposition process involves no solvents, thereby avoiding the impurity contamination commonly found in liquid-phase-based synthesis. The resulting alloy films are highly pure and dense, and the ability to grow single-crystal, polycrystalline, or amorphous films makes PVD a particularly advantageous method for preparing Ni-based solid solution and intermetallic compound films. However, high temperatures may damage the substrate, and the equipment costs are high. Precise preparation of the desired materials requires controlling multiple parameters such as temperature, pressure, gas flow rate, precursor concentration, and substrate surface condition, making the process relatively complex.

View Article Online
DOI: 10.1039/D5NR05514H

Table 1. Comparison of representative synthesis strategies for Ni-based alloy electrocatalysts

Synthetic strategies	Representative methods	Key advantages	Limitations	Product features
Thermal treatment methods	Thermal melting; thermal annealing	High crystallinity; effective for alloy phase formation; suitable for composition tuning; no surface ligand contamination	Possible particle sintering; limited morphology control	Bulk alloys; crystalline nanoparticles
Liquid-phase methods	Hydrothermal/solvothermal method; co-reduction; electrochemical deposition	Good control of particle size and morphology; mild reaction conditions; scalable synthesis	Possible impurities; Sensitive to reaction conditions	Nanoparticles; nanosheets; nanorods; porous structures
Vapor-phase methods	CVD; PVD	High purity; precise thickness and structural control; suitable for model catalysts	Expensive equipment for PVD; relatively low production throughput	Thin films; heterostructures; supported alloys

Overall, different synthetic strategies provide distinct advantages in controlling the composition, morphology, crystallinity, and electronic structure of Ni-based alloy catalysts. Thermal treatment methods are widely used for constructing highly crystalline alloy phases and achieving precise phase regulation, while liquid-phase synthetic strategies offer greater flexibility in controlling nanoscale morphology and particle size under relatively mild conditions. As for vapor-phase techniques, they enable the fabrication of highly uniform thin films and model catalysts with precise structural control. Therefore, selecting an appropriate synthetic method is crucial for tailoring the structural characteristics and catalytic properties of Ni-based alloys. A comparison of the key features, advantages, and limitations of these synthetic routes is summarized in Table 1.

3. Electrocatalytic Applications of Ni-Based Alloy Catalysts

Energy and environmental issues have long been among humanity's most pressing challenges. Ni-based alloys have shown remarkable potential in addressing these challenges across diverse electrocatalytic applications, owing to their active adsorption of various reaction intermediates. This section highlights the latest research progress on electrocatalytic applications of Ni-based alloys, such as hydrogen oxidation, water splitting, O_2 and CO_2 reduction.

3.1 Hydrogen Oxidation Reaction (HOR)

Hydrogen oxidation reaction (HOR) is the anodic half-reaction in hydrogen-oxygen fuel cells, essentially involving the dissociation of hydrogen gas into protons and the release of electrons at the catalyst surface.[119] This reaction proceeds rapidly under acidic conditions but slows significantly under alkaline conditions due to the involvement of additional OH^- ions.[119, 120] Developing high-performance HOR catalysts is crucial for advancing fuel cell technology.

Ni has attracted widespread attention in the field of alkaline HOR due to its ability to adsorb key intermediates (H* and OH*).[121-123] However, Ni alone typically exhibits poor activity, attributed to its excessively strong H adsorption, creating a large Volmer step energy barrier (Fig. 7a).[20, 124] Furthermore, OH species act as reactants in the HOR and can enhance HOR activity via a dual-function mechanism (under alkaline conditions).[125] However, excessive OH adsorption accelerates Ni oxidation, leading to rapid activity decay.[126, 127] Consequently, precise optimization of OH adsorption behavior remains a significant challenge. Alloying, through its associated electronic and strain effects, serves as an effective strategy to enhance HOR activity and stability of Ni. In 2008, Zhuang's group reported that Cr doping weakened H adsorption on Ni, thereby significantly enhancing HOR activity and delivering a maximum power density of 50 mW cm^{-2} at 60 °C in a single membrane-electrode assembly (MEA) of a H_2-O_2 anion exchange membrane fuel cell (AEMFC).[128] Later, various Ni-based alloy catalysts have been developed for HOR, including NiFe,[129] NiCu,[129-131] NiCo,[129] NiCr,[128] NiTi,[132] NiAg,[133] NiMo,[134-137] NiW,[134, 138-140] NiMoW,[141] NiMoCo,[142, 143] NiWCu,[144] NiCuCr,[145] NiCoCuMoW,[146] Ni nitridation (e.g., Ni-H_2-NH_3,[147] Ni_3N[148-150] and Ni_3N/C[150]), and $Ni_{52}Mo_{13}Nb_{35}$ metallic glass.[151] Rational design of multi-metal interactions can effectively suppress hydrogen adsorption and enhance hydroxyl adsorption. For instance, Chen et al. demonstrated that charge transfer among the components of NiMoW alloy yielded significantly higher activity than corresponding binary alloys, achieving a current density of 6.6 mA cm^{-2} at 100 mV vs. reversible hydrogen electrode (RHE), approximately twice that of the Pt/C electrocatalyst.[141] Sheng et al. described that multi-metal interactions in CoNiMo alloys brought Ni-site hydrogen binding energy (HBE) close to Pt (Fig. 7b), resulting in 20-fold higher HOR activity than monometallic Ni.[142] Wang et al. showed that regulating W content in Ni-W alloys modulated the electronic structure of Ni and shifted the potential of zero charge, thereby promoting hydroxyl adsorption. The adsorbed hydroxyl species

View Article Online
DOI: 10.1039/D5NR05514H

disrupted K^+ solvation, releasing free water molecules and optimizing the hydrogen-bond network. As a result, the optimized $Ni_{17}W_3$ alloy outperformed the benchmark Pt/C catalyst in alkaline water electrolysis and exhibited negligible degradation after 10,000 cycles.[140] Moreover, Yu et al. achieved simultaneous regulation of HBE and hydroxyl bond energy (OHBE) by preparing a nitrogen-doped carbon-coated core-shell $Ni_{93}Cu_7$@NC catalyst, which exhibited an outstanding intrinsic activity of 61.0 μA cm^{-2} in alkaline HOR and achieved a peak power density of 381 mW cm^{-2} in a H_2-O_2 single MEA.[152] As illustrated in Fig. 7c, combined experimental characterization and theoretical calculations revealed that the interfacial electron redistribution between the nitrogen-doped carbon shell and the NiCu alloy core produced a dual-regulation effect: it reduced the Ni 4s-H-1s bonding orbital electron occupancy to weaken the HBE, while decreased the Ni $3dz^2$/yz-O-2p antibonding orbital electron density to enhance the OHBE. This precise orbital engineering strategy offers novel insights for designing high-performance non-precious metal catalysts.

Additionally, different active sites can be coupled within the alloy to enhance overall HOR activity. Roy et al. observed a significant increase in HOR activity in the $Ni_{95}Cu_5$ alloy, where Ni primarily facilitated H* adsorption, while Cu sites were responsible for OH* adsorption. Correspondingly, H_2-O_2 single MEA fuel cell tests achieved a power density of 350 mW cm^{-2} at 80 °C.[130] However, Wang et al. revealed a volcano-type relationship between HOR activity and Cu doping concentration, with optimal performance achieved at a Cu doping concentration of 0.4 at%. This discrepancy may stem from variations in active surface area due to microstructural morphology.[131] As shown in Fig. 7d and e, Duan et al. synthesized $MoNi_4$ and WNi_4 with tetragonal nanostructures, which synergistically optimized the adsorption of H* on Ni and OH* on Mo (W), thereby accelerating the Volmer step. The catalyst exhibited a high apparent exchange current density of

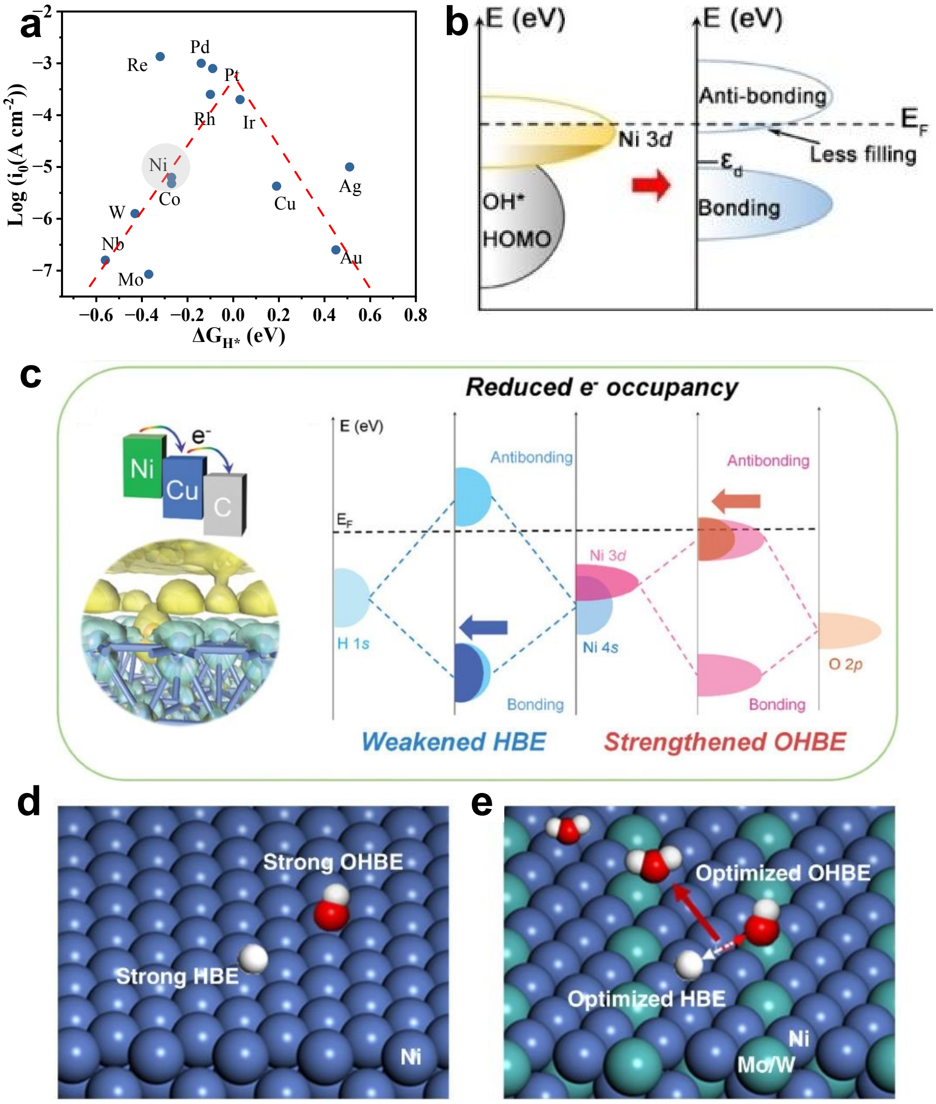

View Article Online
DOI: 10.1039/D5NR05514H

Fig. 7 (a) HER volcano plot showing the relationship between the exchange current density of various metal surfaces and the Gibbs free energy of hydrogen adsorption. Reproduced from ref.[124] with permission from Electrochemical Society, Inc., copyright 2005. (b) Rigid band diagrams of the interaction between Ni 3d orbitals and OH* HOMO with unpaired electrons in Ni 3d. Reproduced from ref.[140] with permission from John Wiley and Sons Ltd, copyright 2024. (c) Schematic illustration of the charge distribution in NiCu@NC, highlighting decreased σ-bonding occupancy and π^* antibonding orbital population, which lead to weakened HBE and enhanced OHBE. Reproduced from ref.[152] with permission from Wiley-VCH, copyright 2024. (d, e) Schematic illustrations of H and OH adsorption on freshly synthesized Ni (d), and Mo(W)Ni_4 alloys (e). Reproduced from ref.[134] with permission from Springer Nature, copyright 2020.

3.41 mA cm^{-2}.[134] However, Ni-W alloys themselves were prone to surface oxidation above 0.1 V. The team further doped Cu into the NiW alloy to form a ternary $Ni_{5.2}WCu_{2.2}$ alloy, which further weakened O adsorption, enabling HOR activity retention without deactivation at 0.3 V.[144] Similarly, Liu et al. proposed that Cu doping optimized H* and OH* adsorption behavior in Ni-M (M = W, Mo, V) alloys, preventing active site oxidation to enhance HOR activity and stability.[153] Furthermore, Du and colleagues synthesized a NiCoCuMoW multi-element alloy, which adjusted the electronic structure of the individual metals and offered multiple active sites. As a result, a high current density of about 11.2 mA cm^{-2} was achieved at an overpotential of 100 mV in 1.0 M KOH.[146]

In summary, the slow reaction kinetics remains a major challenge for HOR, particularly in alkaline media, leading to poor catalytic performance. The introduction of heteroatoms can modulate the binding strengths of H* and OH* on Ni, thus optimizing the catalytic performance. Furthermore, effective alloying strategies should also regulate water activation, highlighting a key characteristic of Ni-based HOR catalysts: their performance depends on the synergistic optimization of H* binding, OH* management, and interfacial electronic structure.

3.2 Hydrogen Evolution Reaction (HER)

Electrocatalytic hydrogen evolution reaction (HER) is the core reaction at the cathode for hydrogen production via water electrolysis.[154] This process involves water or protons acquiring electrons on the catalyst surface to form hydrogen atoms, which ultimately combine to form hydrogen gas.[155] Ni was discovered long ago to exhibit effective HER activity in alkaline environments. Based on a series of experimental results and theoretical calculations, Ni has been found to possess a relatively suitable hydrogen adsorption free energy (ΔG_{H*}) and a relatively high HER exchange current density among non-precious metals.[156] Through voltammetric studies, Miles et al. determined the relative HER activity of non-precious metals as follows: Ni > Mo > Co > W > Fe > Cu.[157]

Ni, as an oxygen-affinity metal with relatively low d-orbital electron occupancy, exhibits excessively strong adsorption of OH* and H* intermediates during catalytic water splitting. This reduces the reaction rate and hinders the sustained production of hydrogen gas.[158] Additionally, Ni-based catalysts are prone to forming surface hydrides during prolonged alkaline HER, leading to catalyst deactivation and reduced stability.[159] Due to the excessively strong hydrogen bonding energy ($E_{b,H}$) on pure Ni surface, its alkaline HER activity remains two orders of magnitude lower than that of commercial Pt/C.[160] The alloying strategy creates broad opportunities for enhancing the catalytic HER performance of Ni.

Extensive research has been conducted on Ni-based alloys for the alkaline HER. As early as the 1980s, Brown et al. investigated various alloy systems for HER and identified the high catalytic activity of NiMo alloy.[161] Subsequently, in the 1990s, Raj et al. prepared various Ni-based bimetallic alloy electrodes via electrochemical deposition, and found that in alkaline environments, the HER activity of Ni-based bimetallic alloy electrodes followed the order of Ni-Mo > Ni-Zn > Ni-Co > Ni-W > Ni-Fe > Ni-Cr > Ni-plated steel.[162] Since then, Ni-Mo alloys have garnered significant attention from researchers.[54, 163] To further enhance the hydrogen evolution performance of NiMo alloys, one approach is to modulate their morphological structure. This can be achieved by creating forms such as porous films,[164] nanoparticles,[165] nanowires,[166] nanosheets,[46] and porous materials,[167, 168] thereby increasing the material's specific surface area and exposing more active sites. Gray and colleagues synthesized Ni-Mo alloy powders that exhibited outstanding HER activity in 2 M NaOH, achieving a current density of 20 mA cm^{-2} at an overpotential of only 70 mV.[165] Wang and colleagues prepared micrometer-length NiMoN/Ni nanowires, which exhibited an overpotential of 22 mV at 10 mA cm^{-2} and a Tafel slope of 101 mV dec^{-1} in 1.0 M KOH, along with excellent stability during multi-step constant-potential tests.[169]

Furthermore, the electronic properties of Ni-Mo-based alloys can be altered through methods such as elemental doping[170] and surface modification[171] to enhance their intrinsic activities. Panek et al. demonstrated that Ti-doped $Ni_{50}Mo_{40}Ti_{10}$ exhibited higher intrinsic activity compared to $Ni_{50}Mo_{50}$.[172] Raj et al. reported that the activity trends for ternary Ni-Mo-based alloys was Ni-Mo-Fe > Ni-Mo-Cu > Ni-Mo-Zn > Ni-Mo-Co ≈ Ni-Mo-W > Ni-Mo-Cr. The Ni-Mo-Fe electrode achieved 300 mA cm^{-2} at an overpotential of 187 mV and sustained hydrogen evolution for 1500 hours.[173] However, compared with Pt, it still suffers from relatively high overpotentials and low energy utilization efficiency, highlighting the need for further efforts to develop high-performance catalysts.[174] Zhou et al. prepared NiMoCu alloys through Cu doping, significantly mitigating the OH poisoning of NiMo.[175] As illustrated in Fig. 8a and b, their HER activity exceeded those of NiMo and Pt/C by nearly 19.5- and 6.9-fold, respectively. Theoretical research indicated that NiMoCu separated H* and OH* adsorption sites (Ni-Cu for H* and Mo for OH*), effectively mitigating H* site blocking. This separation optimized short-range adsorption of various intermediates, thereby enhancing reaction kinetics.

Normally it is believed that introducing surface-adsorbed species to modify a catalyst may reduce catalytic activity by covering active sites. However, surface adsorbates also hold the potential to improve the interfacial electronic structure of catalysts and enhance their catalytic performance. Gao et al.

View Article Online
DOI: 10.1039/D5NR05514H

discovered that introducing diamines (such as ethylenediamine) onto the surface of NiMo nanoparticles significantly reduced electrical resistance and optimized the interfacial electronic structure.[171] This resulted in a 268 mV decrease in overpotential at 10 mA cm^{-2} compared to the unmodified state, substantially enhancing catalytic activity. Zhang et al. constructed NiMo alloys dispersed on the MoO_2 surface by controlling the outward diffusion of Ni atoms through annealing $NiMoO_4$ precursors. Experimental and theoretical analyses confirmed that the accelerated Tafel step promoted hydrogen evolution on the $MoNi_4$ electrocatalyst. Consequently, the catalyst displayed an overpotential of 15 mV at 10 mA cm^{-2} and a Tafel slope of 30 mV dec^{-1} in 1 M KOH, comparable to those of Pt electrocatalysts. (Fig. 8c).[176]

Although numerous Ni-Mo-based alloy electrocatalysts with outstanding alkaline HER catalytic performance have been developed, their long-term stability requires further investigation.[177] It has been revealed that during the HER process, Ni-Mo alloys form Ni-enriched surfaces where Ni readily converts to $Ni(OH)_2$, while Mo primarily exists as MoO_3 on the electrode surface.[178, 179] Studies have also shown that Mo leaches in the form of MoO_4^{2-}, increasing the material's surface area and thereby enhancing its reactivity.[38, 180] Du et al. observed that during the alkaline HER process catalyzed by Ni_4Mo nanorods, free Mo species in the electrolyte gradually increased within the first 4 hours, with approximately 40% of metallic Mo dissolving. Under non-potential conditions, only 7% of Mo dissolved within the same timeframe. This indicates that at alkaline hydrogen evolution potentials, Mo readily undergoes electrochemical oxidation to form MoO_4^{2-} and dissolves into the electrolyte (Fig. 8d).[181] Interestingly, the authors further proposed that the dissolved MoO_4^{2-} species can re-adsorb onto the electrode surface and undergo polymerization to form dimeric $Mo_2O_7^{2-}$ species, which in turn promote the HER activity of metallic Ni.

In addition to Ni-Mo-based alloys, broader Ni-based alloys have also been developed for HER, including Ni-W,[91, 182] Ni-Mn,[183] Ni-Te,[184] Ni-Cu,[47, 185] Ni-Co,[49, 186] Ni-Al,[187] Ni-Zn,[80] Ni-Ti,[188] and Ni-Co-Al.[61] Xie et al. synthesized Ni-M (M = Mo, Ge, Sn) bimetallic alloy nanosheets, which significantly enhanced the HER activity rather than the pure Ni.[189] Ren and colleagues prepared P-CuNi alloy catalysts with P-Ni bonds through P doping. This treatment converted the nanoparticles into sub-nanoscale sheet structures, markedly increasing the electrochemically active surface area and creating additional active sites. The resulting P-CuNi alloys showed excellent HER performance in 1.0 M KOH, achieving an overpotential of 50 mV at 10 mA cm^{-2} and maintaining outstanding stability during extended operation.[88] Halilu et al. proposed a NiFe/NF alloy with enriched (111) orientation as an HER electrocatalyst and introduced an analysis method for deconvoluting and measuring charge transfer relaxation times in water-splitting electrocatalysts using custom-developed Python software. The electrocatalyst demonstrated excellent HER performance, reaching a current density above 800 mA cm^{-2}, an overpotential of 133 mV, and a hydrogen turnover frequency of 2.8×10^{12} s^{-1}, while maintaining stable operation for over 100 h.[79]

In summary, Ni-based alloy catalysts have shown great promise for HER due to their tunable hydrogen adsorption properties and improved reaction kinetics. For example, Ni-Mo based alloys generally exhibit superior activity in alkaline media due to their ability to accelerate water dissociation and optimize hydrogen adsorption,[162, 165] whereas Ni-Fe systems typically show lower HER activity because Fe favors the moderate adsorption of oxygen-related intermediates.[162] In addition, alloying Ni with elements such as Cu or Co can modulate its electronic structure and improve conductivity, but their impact on hydrogen binding is relatively weaker compared with Mo-containing systems.[47, 49, 185, 186] From a structural perspective, nanostructured alloys with defects, porous architectures, or heterointerfaces consistently outperform bulk counterparts by exposing more active sites and facilitating charge transfer. These comparisons indicate that the structural factors such as phase composition, defect density, heterointerfaces, and nanoscale morphology play crucial roles in determining HER activity and durability.

3.3 Oxygen Evolution Reaction (OER)

Electrocatalytic oxygen evolution reaction (OER) is the primary anodic process in electrochemical energy conversion systems, including water splitting and metal-air batteries.[190] This process involves water molecules losing electrons on the catalyst surface to generate oxygen gas. OER typically exhibits slow kinetics, involving multi-electron transfer and intermediate adsorption,[191] thus requiring catalysts with high activity and stability. Ni is commonly used for constructing OER catalysts, however, its high chemical reactivity makes Ni-based electrocatalysts, whether in elemental or alloy forms, cannot be directly employed in harsh acidic or alkaline electrolytes under OER potentials. To address this issue, embedding or assembling them into relatively inert matrix materials, such as carbon, can significantly enhance their stability.[192] Wang and collaborators synthesized NiFe alloy nanoparticles with different crystal phases encapsulated in N-doped carbon layers. Among these, the NiFe alloy catalyst with an hcp phase achieved a current density of 10 mA cm^{-2} at an overpotential of only 226 mV.[193]

However, numerous studies indicate that alloys are not the true active phases for OER and typically cannot remain stable under OER conditions.[191] Instead, they are ultimately oxidized on the surface (or entirely) into hydroxide (or hydroxyl oxide) active phases.[194-196] However, alloys still offer advantages as pre-catalysts due to the presence of metal cores, which possess higher electronic conductivity than oxides, hydroxides, and oxyhydroxides, thus facilitating rapid electron transfer during the OER process.[197]

As shown in Fig. 8e and f, a series of transition metal alloy nanoparticles, including FeCo, FeMn, NiFe, NiCo, MnCo, and NiMn, exhibit significantly higher OER activity than their corresponding monometallic counterparts. Among these catalysts, NiFe demonstrates the optimal activity and stability.[198] As mentioned above, NiFe alloys undergo in situ conversion into the corresponding (oxy)hydroxides during the OER, which complicates the identification of the actual active sites in alloy electrocatalysts.[195] Chen et al. observed that NiLa alloys underwent conversion to hydroxides during OER. The presence of $La(OH)_3$ prevented the aggregation of $Ni(OH)_2$ and promoted the formation of the active γ-NiOOH phase, thereby enhancing OER stability and activity (Fig. 8g). As a result, the overpotential at 100 mA cm^{-2} was decreased by 104 mV to 322 mV compared with the original NiLa phase.[199] Furthermore, in addition to conversion into hydroxides, certain elements in alloys may dissolve into the electrolyte. Moderate and selective metal leaching can generate metal vacancies, induce surface reconstruction, and tailor the morphology and electronic structure. For instance, during OER, Ge in NiGe alloys transformed into GeO_3^{2-} and leached into the electrolyte while simultaneously promoting the formation of the highly active γ-NiOOH phase (Fig. 8h).[200] Under anodic polarization, the Mo in NiMo alloys underwent dealloying, promoting the transformation of Ni to NiOOH. The residual Mo tuned the electronic structure of NiOOH, while dissolved Mo formed

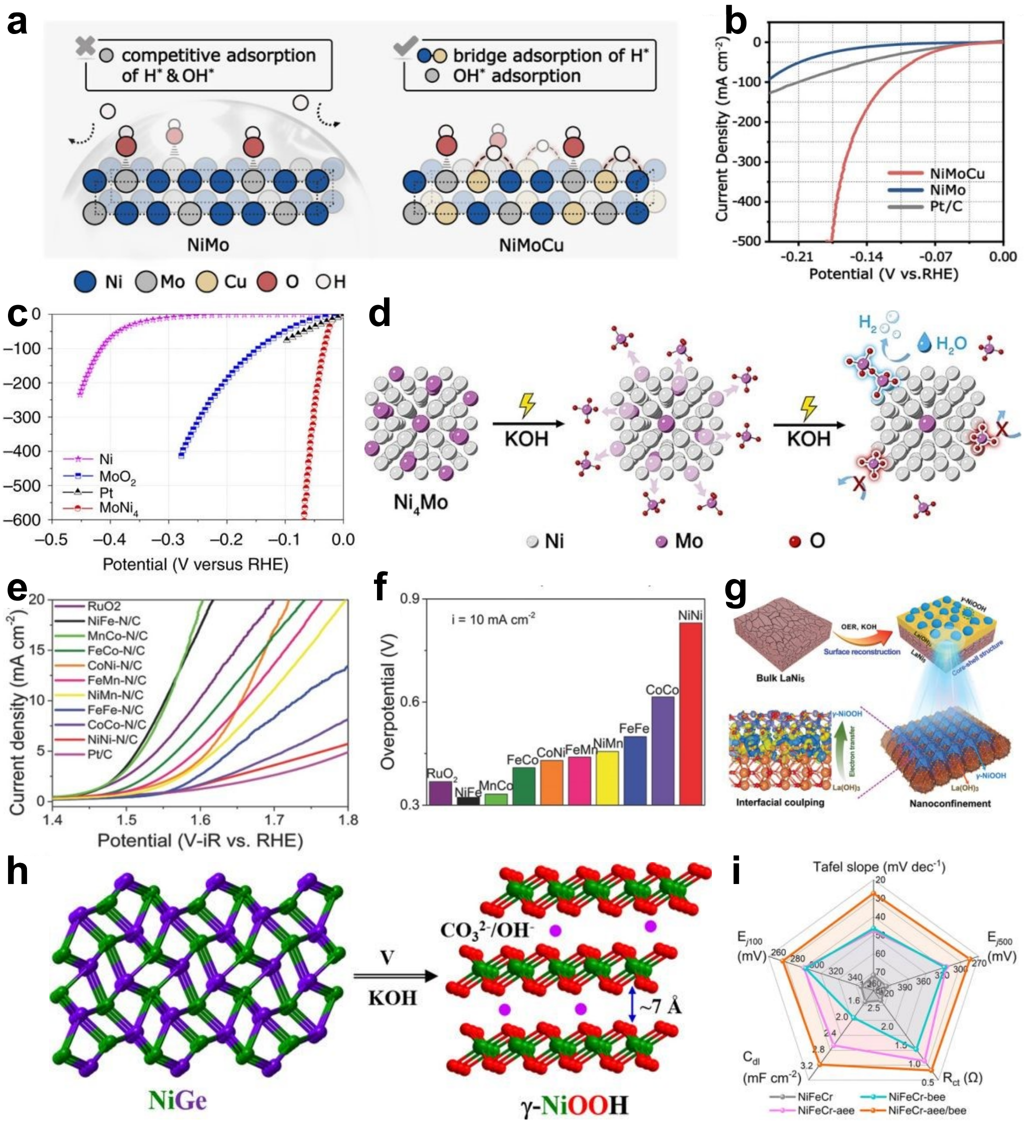

Fig. 8 (a) Schematic illustration of the competitive adsorption of OH* and H* on the Mo site of the NiMo alloy, and the separated adsorption of OH* and H* on the Mo site and Ni-Cu dual site of the NiMoCu alloy. (b) Linear sweep voltammetry (LSV) curves of NiMoCu, NiMo, and Pt/C. Reproduced from ref.[175] with permission from Wiley-VCH, copyright 2025. (c) Polarization curves of the $MoNi_4$ electrocatalyst supported on MoO_2 cuboids, compared with pure Ni nanosheets and MoO_2 cuboids deposited on Ni foam. Reproduced from ref.[176] with permission from Springer Nature, copyright 2017. (d) Schematic illustration of the role of Mo in the Ni_4Mo alloy during alkaline HER. Reproduced from ref.[181] with permission from John Wiley and Sons Ltd, copyright 2021. (e) LSV polarization curves for different binary alloy samples, Pt/C, and RuO_2 in O_2 saturated 0.1 M KOH, (f) overpotential at a current density of 10 mA cm^{-2}. Reproduced from ref.[198] with permission from Wiley-VCH, copyright 2017. (g) Schematic illustration of how La enhances the OER performance of the $LaNi_5$ precatalyst. Reproduced from ref.[199] with permission from Wiley-Blackwell, copyright 2023. (h) Crystal structures of NiGe and electrochemically formed γ-NiOOH. When a potential is applied in an alkaline KOH electrolyte, Ge is fully dissolved, resulting in the formation of γ-NiOOH. Reproduced from ref.[200] with permission from John Wiley and Sons Ltd, copyright 2021. (i) Radar graph comparing the overpotentials (at 100 and 500 mA cm^{-2}), Tafel slope, charge transfer

resistance (R_{ct}), and double layer capacitance (C_{dl}) for NiFeCr-aee/bee. Reproduced from ref.[201] with permission from Royal Society of Chemistry, copyright 2025.

View Article Online
DOI: 10.1039/D5NR05514H

MoO_4^{2-}, which repelled Cl^- ions from the catalyst surface and facilitated selective seawater oxidation.[202] Ni_2Si transformed into the $Ni^{3+}O_xH_y$ active phase after the OER process. The dissolution of Si (via oxides, hydroxides, or polysilicates) endowed the $Ni^{3+}O_xH_y$ phase with a more porous structure featuring distorted layered sheets, facilitating electrolyte permeation. The activated form of the catalyst delivered a current density of 100 mA cm^{-2} at an overpotential of 348 mV.[203] Kumar et al. also demonstrated that post-reaction surfaces of NiSi and Ni_2Si transformed into $Ni^{3+}O_xH_y$ species with Si dissolving into the electrolyte, while the Ni-Si core remained stable and enhanced charge conduction.[63] Samanta et al. synthesized ultrafine monodisperse NiZn intermetallic nanoparticles, whose atomic-scale synergistic effects between Ni and Zn enabled excellent OER performance with a low overpotential of 283 mV at 10 mA cm^{-2} and a small Tafel slope of 73 mV dec^{-1}, along with remarkable stability and durability.[204]

Additionally, reactivity of Ni-based alloys can be enhanced by increasing their active surface areas. Jović et al. obtained a rough NiSn coating on Ni mesh by increasing the electrodeposition current density, which significantly boosted the electrochemically active surface area. This resulted in an apparent activity for OER that was substantially higher than that of Ni electrode. However, the authors concluded that the Sn sites in the NiSn electrode did not play a significant role in the OER kinetics.[205] Chen and colleagues prepared CoNi alloy nanoparticles uniformly embedded in a hollow nitrogen-doped carbon matrix. The hollow structure increased the exposure of active sites, while strong electron interaction between Ni and Co in the alloy promoted charge transfer and lowered the energy barrier for the OER, resulting in an overpotential of 223 mV at a current density of 10 mA cm^{-2}.[57] Zhang and colleagues developed a multi-step etching strategy to precisely control dealloying and self-reconstruction of NiFeCr alloys, producing NiFe-OOH@Ni/Fe-Cr_2O_3@NiFeCr (NiFeCr-aee/bee) catalysts. In this structure, Cr played a dual role by forming a passivating Cr_2O_3 layer that limited excessive Fe and Ni dissolution and by acting as a sacrificial element to create a porous framework. The resulting catalyst demonstrated excellent OER performance in 1 M KOH, with overpotentials of 284 and 292 mV at current densities of 500 and 1000 mA cm^{-2}, respectively, while maintaining stable operation for more than 1000 hours at 500 mA cm^{-2} (Fig. 8i).[201]

Additionally, high-entropy alloys have also attracted significant attention from researchers. Although high-entropy alloys theoretically exhibit greater stability, their surfaces still oxidize into (oxy)hydroxides during the OER process,[206-208] posing challenges for elucidating active sites and reaction mechanisms. A $Fe_{0.5}CoNiCuZn_x$ high-entropy alloy catalyst has been reported, whose excellent OER activity was attributed to the in situ formation of a multi-oxide layer composed of Fe_3O_4, Co_3O_4, CuO, NiO, and ZnO, as well as the synergistic effects of its multicomponent structure. The optimal sample exhibited a low overpotential of 340 mV at 10 mA cm^{-2}.[209] Mei et al. reported a FeCoNiMo high-entropy alloy catalyst in which Mo transferred electrons to Fe, Co, and Ni, leading to weakened OH adsorption and thereby enhanced OER performance. As a result, the FeCoNiMo high-entropy alloy catalyst achieved an overpotential of 250 mV at a current density of 10 mA cm^{-2} in alkaline media, 89 mV lower than that of IrO_2.[210] Additionally, a self-supporting FeCoNiCrMo high-entropy alloy has been reported. The authors proposed that Mo underwent rapid oxidation and dissolution into the electrolyte, triggering concomitant Cr leakage and leaving reconstructed active NiFeCo oxyhydroxide nanostructures on the surface. Here, Mo species were absorbed and/or incorporated into the active layer as MoO_4^{2-} anions to accelerate $Ni^{2+/3+}$ redox transitions, thereby promoting the formation of the active β-NiOOH phase. Cr atoms existed as dopants at low abundances within the surface hydroxide/oxyhydroxide layer and could serve as additional active sites. The optimal catalyst exhibited overpotentials of 303 and 372 mV to achieve current densities of 100 and 700 mA cm^{-2}, respectively, and retained its activity for 120 h in alkaline media.[211] Chen et al. synthesized nano-flower-shaped ZnCoNiFeV alloys, and reported that the introduction of V can modulate the electronic structures of Co, Ni, and Fe, induce the formation of highly active Ni centers, and lower the reaction potential barrier for the OER.[212]

Overall, the application of Ni-based alloy catalysts in OER demonstrates that alloying is an effective strategy to modulate the adsorption energetics of oxygen-containing intermediates and enhance the redox activity of Ni sites. In many cases, alloying elements not only optimize the electronic structure of the pre-catalyst but also influence the surface reconstruction behavior under anodic conditions, which is closely related to the formation of real active species. Therefore, the OER performance of Ni-based alloys is strongly governed by both the pre-catalyst structure and its dynamic evolution during operation.

3.4 Oxygen Reduction Reaction (ORR)

Electrocatalytic oxygen reduction reaction (ORR) is a key reaction at the cathode of fuel cells and metal-air batteries. The process involves oxygen molecules acquiring electrons on the catalyst surface and being reduced to water or hydroxide ions.[213] ORR involves multi-electron transfer and multi-step reaction pathways, exhibits slow kinetics, and typically relies on Pt-based catalysts.[214] Given the high cost and scarcity of Pt, efforts to reduce the excessive reliance on precious metals for ORR catalysts have led to increased focus on developing non-precious metal catalysts alongside Pt-based alloy catalysts. Compared to Pt-based catalysts, non-precious metal catalysts offer distinct advantages in terms of abundant global resources and low cost, though improvements in catalytic activity and stability remain necessary.[215, 216]

The four-electron ORR refers to the direct reduction of O_2 to H_2O (or OH^- in alkaline media), which is highly desirable for

View Article Online
DOI: 10.1039/D5NR05514J

applications in fuel cells and metal-air batteries.[217] Research on Ni-based non-precious metal alloys as 4-electron ORR electrocatalysts has primarily focused on FeNi[218-220] and NiCo[221, 222] alloys. Loading these catalysts onto carbon materials can significantly enhance corrosion resistance, reduce alloy particle size, and improve thermodynamic stability. Furthermore, doping carbon materials with heteroatoms, such as pyridine nitrogen-induced Lewis-base carbon atoms, favors ORR due to adjustments in electronic structure.[218] Based on this approach, Fu and colleagues modified NiCo alloy nanoparticles on nitrogen-doped carbon nanofibers to prepare a hybrid catalyst. The sample containing 39 wt% NiCo alloy showed the highest catalytic activity, with a Tafel slope of 65 mV dec^{-1}.[221] Wu et al. embedded FeNi alloys into nitrogen-doped carbon with tunable architectures. Benefiting from abundant active sites provided by the FeNi alloys and a stable carbon matrix, the catalyst exhibited an ORR onset potential of 0.95 V and a half-wave potential of 0.86 V, approaching those of commercial Pt/C (Fig. 9a).[219]

Electrocatalytic two-electron oxygen reduction, which converts low-value oxygen into high-value-added hydrogen peroxide, has become a research hotspot.[223] Liu et al. developed a BiNi alloy electrocatalyst supported on carbon

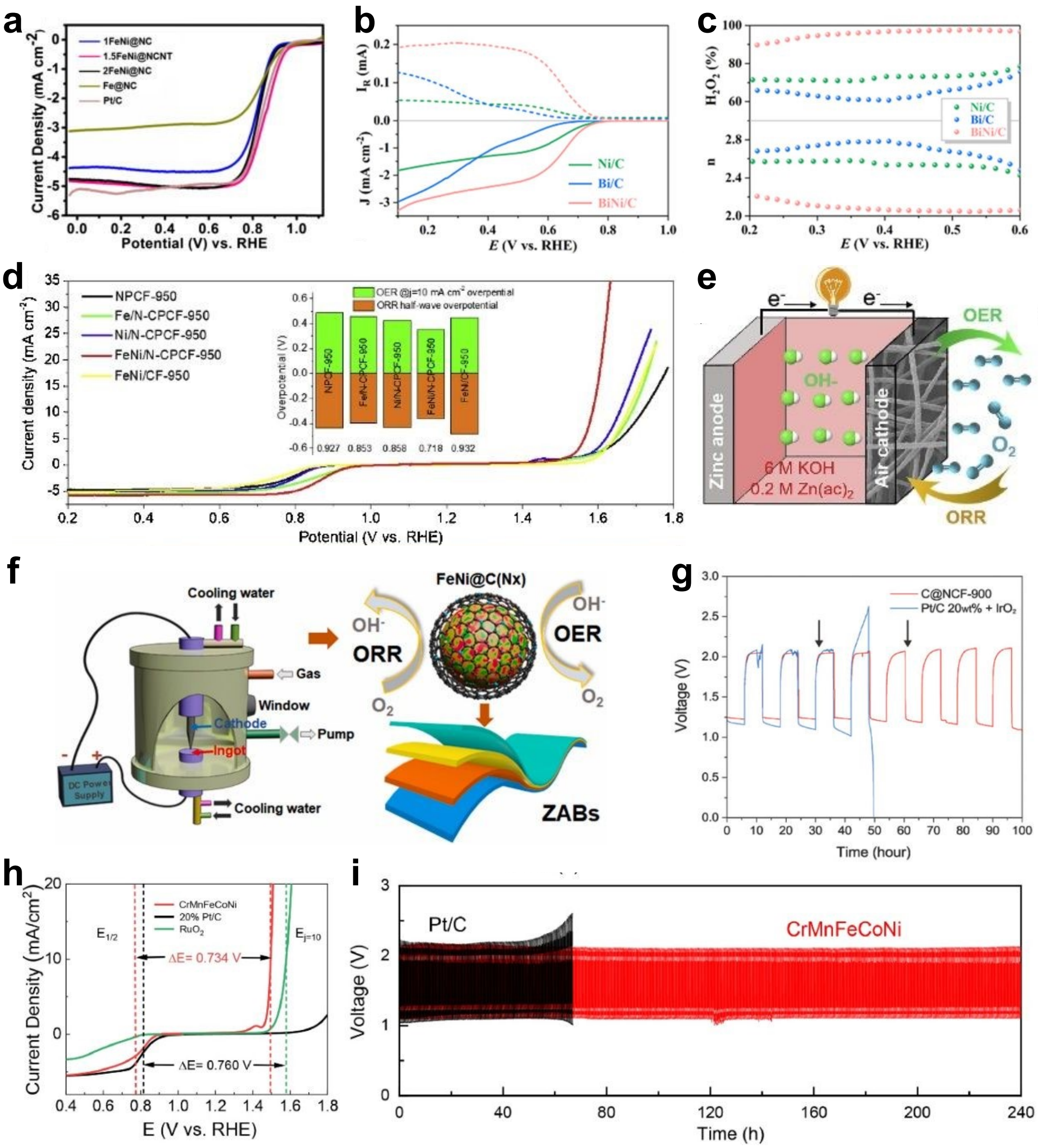

Fig. 9 (a) LSV curves of the NiFe alloy samples and Pt/C measured at 1600 rpm with a scan rate of 10 mV s^{-1} in 0.1 M KOH. Reproduced from ref.[219] with permission from Academic Press Inc., copyright 2020. (b) LSV curves, (c) electron transfer number (n) and H_2O_2 selectivity (%) of Bi/C, Ni/C, and BiNi/C in alkaline electrolytes. Reproduced from ref.[224] with permission from American Chemical Society, copyright 2025. (d) Polarization curves of FeNi/N-CPCF-950 and other reference catalysts. The inset presents the corresponding overpotential difference between $E_{1/2}$ and $E_{j=10}$. (e) Schematic illustration of the liquid zinc-air battery configuration. Reproduced from ref.[225] with permission from Elsevier, copyright 2020. (f) Schematic illustration of the construction of core-shell

View Article Online
DOI: 10.1039/D5NR05514H

nitrogen-doped carbon-coated FeNi nanostructures as bi-functional catalysts for flexible solid-state Zn-air battery. Reproduced from ref.[226] with permission from Elsevier Ltd, copyright 2023. (g) Electrochemical performance of C@NCF-900 and Pt/C electrocatalysts in both half-cell and Zn-air full-cell configurations under ambient air. The black arrows indicate electrolyte refilling with 6 M KOH containing ZnO. Reproduced from ref.[227] with permission from Wiley-Blackwell, copyright 2018. (h) Bifunctional LSV curves for ORR and OER measured on Pt/C, RuO_2, and CrMnFeCoNi. (i) Galvanostatic discharge and charge curves with 10 min discharge and 10 min charge cycles at a current density of 8 mA cm^{-2}. Reproduced from ref.[228] with permission from Elsevier, copyright 2023.

nanosheets (BiNi/C), which exhibited outstanding $2e^-$ ORR performance with H_2O_2 production, featuring an onset potential of 0.76 V vs. RHE and H_2O_2 selectivity as high as 98% (Fig. 9b and c). Experimental and theoretical calculations demonstrated that Bi modulated the electronic structure of Ni in the BiNi alloy through a “dual isolation” effect involving both physical and electronic isolation.[224] In another case, CoNi alloy nanoparticles were supported on nitrogen-doped mesoporous hollow carbon nanospheres, demonstrating excellent $2e^-$ ORR performance in acidic media. The authors proposed that charge redistribution between Co and Ni atoms could lower the reaction energy barrier for *OOH conversion to H_2O_2, thereby promoting reaction kinetics.[229]

The composition, size, and carbon coating layer of Ni-based alloy catalysts have been finely modulated to achieve full exposure of active sites and optimized adsorption energy for oxygen reaction intermediates. Consequently, bifunctional catalysts exhibiting activity for both ORR and OER have been further developed for use in rechargeable metal-air batteries.[230]

In oxygen electrode reactions, a core-shell structure is often formed, with a carbon layer as the shell and an alloy as the core. The stable shell layer in this core-shell structure effectively protects the alloy from corrosion during electrochemical reactions.[231] For example, Wang et al. proposed embedding Ni-Fe alloy nanoparticles into nitrogen-doped carbon nanotube-coated porous carbon fibers, whose potential gap (ΔE), defined as the difference between the OER potential at 10 mA cm^{-1} and the ORR half-wave overpotential, was as low as 0.72 V, indicating excellent bifunctional ORR/OER activity (Fig. 9d and e).[225] Miao et al. reported a novel nitrogen-doped carbon-coated FeNi core-shell electrocatalyst as highly efficient bifunctional electrocatalysts for both ORR and OER. Specifically, the catalyst exhibited an OER overpotential of 326 mV, outperforming RuO_2 (405 mV), while the ORR proceeded predominantly via a $4e^-$ pathway. Furthermore, an all-solid-state Zn-air battery using this electrocatalyst achieved a high open-circuit voltage of 1.394 V and a peak power density of 59.7 mW cm^{-2} (Fig. 9f).[226] Additionally, Ni-based alloy catalysts containing multiple elements have also been reported. Nam et al. proposed introducing Fe into NiCo alloys to construct NiCoFe catalyst. DFT calculations revealed that NiCoFe ternary alloys exhibited optimized electrocatalytic performance compared with NiCo binary alloys for both ORR and OER. When applied in zinc-air batteries, NiCoFe outperformed the benchmark Pt/C (20 wt%) and IrO_2 catalyst mixture, maintaining stable cycling for over 100 h at a depth of discharge of 58% (Fig. 9g).[227] Lu et al. also discovered that encapsulating a NiCoFe alloy core within a graphite carbon shell yielded a versatile catalyst exhibiting excellent activity for the OER, ORR, and HER. The encapsulation of the NiCoFe alloy core induced electronic structure changes in the outer graphitic carbon shell, thereby modulating the binding strength of reaction intermediates and enhancing catalytic activity.[232] He et al. prepared a CrMnFeCoNi high-entropy alloy, which exhibited pronounced lattice distortion and unique surface electronic states, thereby delivering outstanding bifunctional catalytic activity toward both OER and ORR. DFT calculations revealed that Cr doping in MnFeCoNi and the defect structure of high-entropy alloys both reduced the energy barrier for *O to form *OOH. As shown in Fig. 9h and i, CrMnFeCoNi exhibited outstanding ORR/OER performance with a ΔE of 0.64 V, coupled with excellent electrochemical stability. Due to its exceptional thermodynamic stability and corrosion resistance, CrMnFeCoNi even eliminated the need for carbon supports, thereby avoiding issues of carbon corrosion and inherent active site depletion.[228]

Overall, the ORR performance of Ni-based alloy catalysts is strongly governed by the nature of alloying elements and the resulting electronic structure modulation. For instance, Ni-Fe[219] and Ni-Co[221] alloys can enhance oxygen adsorption and facilitate O-O bond activation, generally favoring the four-electron pathway toward H_2O. In contrast, Ni-Bi alloys tend to shift the reaction toward the two-electron pathway and promote H_2O_2 production when the binding strength is appropriately tuned.[224] These comparisons indicate that optimizing the adsorption energetics of oxygen intermediates is essential for achieving high ORR activity and selectivity. Besides, Ni-based alloy catalysts have also demonstrated great potential as bifunctional catalysts for both ORR and OER, which are critical for rechargeable metal-air batteries. In such systems, a key challenge lies in simultaneously balancing the adsorption of oxygenated intermediates for both reactions, as ORR and OER often demand different optimal binding strengths. The introduction of Fe into NiCo systems or the construction of high-entropy alloys has been proven effective in reducing potential gaps (ΔE) by tuning electronic structure and inducing lattice distortion, indicating improved ORR/OER bifunctional activity.[227] Briefly, alloy engineering provides an effective strategy to optimize the catalytic performance by tuning the electronic structure and surface coordination environment, thereby enabling a compromise between ORR activity and OER performance.

3.5 Carbon Dioxide Reduction Reaction (CO_2RR)

Electrocatalytic CO_2 reduction reaction (CO_2RR) is the process of reducing CO_2 into high-value-added products such as CO, formic acid, hydrocarbons, or alcohols through multi-electron transfer on a catalyst surface.[233] This reaction involves complex reaction pathways and competition among different intermediates, requiring catalysts with high activity, selectivity, and stability. As a vital upstream chemical feedstock, CO is extensively applied in chemical, metallurgical, and pharmaceutical industries, possessing significant economic value. Moreover, the reaction

View Article Online
DOI: 10.1039/D5NR05514H

pathway for generating CO via CO_2RR is relatively straightforward (involving a two-electron/proton reaction), exhibiting high catalytic efficiency and thus strong industrialization potential.[234] However, the application of metallic Ni in CO_2RR for CO production is constrained by its excessively strong binding energy with the *CO intermediate (Fig. 10a).[235]

Although numerous studies have employed surface structure modification strategies to enhance the CO selectivity of Ni nanoparticles, the reported Ni nanoparticles catalysts remain constrained by high overpotentials, poor stability, low Faradaic efficiency (FE), and narrow usable voltage ranges, thereby failing to adequately meet practical application requirements.[236]

By leveraging the alloying effects between Ni and other metals, the d-band centers in Ni-based alloys can be effectively controlled, enabling precise regulation of the binding energies for *COOH and *CO intermediates. This approach can guide the efficient synthesis of high-performance Ni-based alloy catalysts.[15, 237, 238] For instance, Zhang et al. observed that the d-band center in Co_xNi_{1-x} nanoalloys shifted upward with increasing Co content, leading to significant changes in the binding energy and reaction free energy (ΔG) of key intermediates (*COOH, *CO, and *H). The $Co_{0.75}Ni_{0.25}$ alloy supported by N-doped carbon nanofibers ($Co_{0.75}Ni_{0.25}$/N-C NFs) exhibited optimal performance, promoting CO_2RR while suppressing hydrogen evolution. The optimal $Co_{0.75}Ni_{0.25}$/N-C NFs exhibited a high FE_{CO} of 85.0% and a current density of -13.4 mA cm^{-2} at -0.9 V vs. RHE in 0.5 M $NaHCO_3$.[239] In addition to NiCo alloys, Jia's group investigated the CO_2RR performance of nitrogen-doped carbon-supported NiFe nanoparticles. They discovered that adjusting the Ni/Fe elemental ratio could regulate the CO/H_2 ratio of reduction products. When the Fe/Ni ratio reached 2:1, the CO/H_2 ratio in the synthesis gas achieved optimal performance (1.2-2.9).[240] Qiao' s group developed a graphite-coated Ni-Cu bimetallic nanoparticle catalyst for highly efficient CO_2RR to produce CO (Fig. 10b).[241] It was revealed that NiCu catalysts with bimetallic active sites exhibited superior catalytic performance compared to single-metal Ni catalysts. X-ray absorption near-edge structure (XANES) analysis indicated that the introduction of Cu elevated the oxidation state of Ni within the alloy. Modulating the Cu content in the alloy

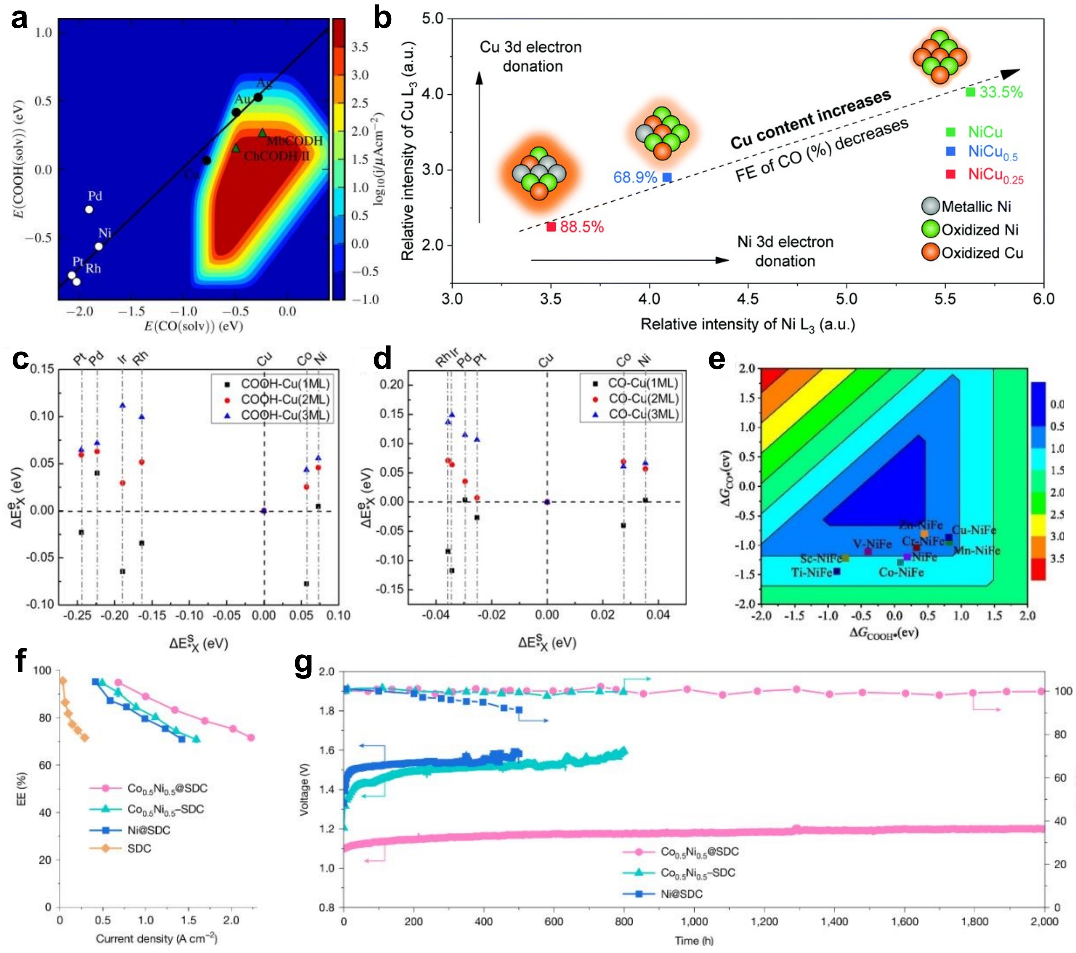

Fig. 10. (a) Kinetic volcano plot for CO formation at an overpotential of 0.35 V on the (211) steps of transition metals. Reproduced from ref.[235] with permission from American Chemical Society, copyright 2013. (b) Electron donation and CO selectivity trends as the Cu content increases in $NiCu_x$. The glow illustrates the 3d electron density in the molecular model, with a stronger glow indicating higher electron density. Reproduced from ref.[241] with permission from Royal Society

View Article Online
DOI: 10.1039/D5NR05514H

of Chemistry, copyright 2020. (c, d) Strain effect versus ligand effect of Cu alloy on tuning the adsorption energy of key intermediates of *COOH (c) and *CO (d) during CO_2RR. Reproduced from ref.[242] with permission from American Chemical Society, copyright 2017. (e) Overpotential of CO formation on different ternary transition metal-doped TM-NiFe catalyst as a function of ΔG_{COOH*} and ΔG_{CO*}. Reproduced from ref.[243] with permission from Elsevier BV, copyright 2023. (f) Energy efficiencies at different current densities for $Co_{0.5}Ni_{0.5}$@SDC. (g) Stability tests of $Co_{0.5}Ni_{0.5}$@SDC at a constant current density of 1.0 A cm^{-2}. Reproduced from ref.[244] with permission from Springer Nature, copyright 2025.

regulated the electronic contribution of Ni's 3d orbitals, thereby effectively controlling the CO selectivity of the alloy, achieving a maximum FE_{CO} value of 88%. Tan and colleagues prepared Cu_xNi_y alloy nanoparticles embedded in a nitrogen-carbon network, showing high CO_2 adsorption capacity. The catalyst effectively converted CO_2 to CO at -0.60 V vs. RHE, achieving a maximum FE_{CO} of 94.5% and a current density of 18.8 mA cm^{-2}.[245] To further enhance the catalytic efficiency of NiCu alloys, Liu's group utilized a metal-organic framework compound (ZIF-8) as a template to prepare nitrogen-doped carbon-supported NiCu nanoparticles. This catalyst exhibited excellent CO selectivity over a broad voltage range from -0.3 to -0.8 V vs. RHE, with a maximum FE_{CO} value reaching 99.7%.[246] In addition to the electronic structure changes induced by ligand effect (changes caused by neighboring atoms), strain effect in alloy materials can also influence catalytic performance. Strain effect arises from lattice distortion, which modifies the electronic properties and adsorption behavior of surface atoms.[247] Yang's group investigated the different effects of ligand interactions and strain effects on the adsorption energies of *COOH and *CO intermediates in core-shell Cu-Ni alloys using DFT, as illustrated in the Fig. 10c and d.[242] For CuNi alloys, when the outer Cu layer thickness was one monolayer (1 ML), the strain effect dominated the modulation of the adsorption energies of *COOH and *CO intermediates, with values of 0.074 and 0.034 eV, respectively. These values were significantly higher than those associated with the ligand effect (0.006 eV for *COOH and 0.002 eV for *CO). As the number of outer Cu layers increased, the influence of the ligand effect on the adsorption energies of both intermediates gradually became more pronounced.

Multi-element alloys can further modulate catalyst activity and stability, as well as selectivity toward products. Liu et al. designed and synthesized a ternary transition metal-doped TM-NiFe catalyst by creating an active two-dimensional volcano plot (Fig. 10e), and screening highly efficient catalysts via DFT calculations. The catalytic performance and reaction mechanism of the TM-NiFe catalyst for CO_2 conversion to CO and HCOOH were examined. Weak CO adsorption on the Zn-NiFe surface favored CO formation. V-NiFe displayed balanced selectivity between CO and H_2, making it a promising catalyst for syngas production. In the Cr-NiFe catalyst, the relatively high negative charge at the active site and the low d-band center of Cr atoms promoted HCOOH formation through the COOH* pathway at a low overpotential of 0.080 V vs. RHE. Furthermore, on the Cr-NiFe catalyst, the CO_2RR conversion to HCOOH significantly suppressed both HER and CO_2RR conversion to CO.[243] Xu et al. synthesized an inorganic/organic hybrid high-entropy alloy zeolite imidazole framework (HE-ZIF) via entropy-driven synthesis, featuring random distribution of five metals (i.e., Zn, Co, Cd, Ni, and Cu) within its structure. The study revealed that compared to ZIF-8, HE-ZIF exhibited enhanced electrocatalytic reduction of CO_2 to carbonate, attributed to the synergistic interaction of the five metals.[248]

Despite extensive research in the field of low-temperature CO_2 electrolysis (below 100 °C), the technology still faces numerous challenges, including low system-level energy efficiency and limited operational lifespan.[249, 250] High-temperature CO_2 electrolysis at 600-1000 °C within solid oxide electrolysis cells has emerged as an ideal solution for CO_2 utilization.[250, 251] However, high temperatures exacerbate catalyst agglomeration and sintering issues. It has been revealed that incorporation of Fe into Ni significantly enhanced the current density for electrochemical CO_2 reduction to CO. At 1.6 V and 800 °C, the Ni-Fe (9:1) cathode achieved a current density of 1.84 A cm^{-2}. This enhanced activity was attributed to the stabilization of fine Ni particles by Fe addition, which suppressed agglomeration and sintering and consequently reduced diffusion resistance.[252, 253] Hu and coworkers suggested that encapsulating active alloys within inert oxides can both prevent alloy agglomeration and generate rich interfaces, thereby overcoming the usual trade-off between activity and stability.[244] The team developed a NiCo alloy catalyst encapsulated with Sm_2O_3-doped CeO_2 ($Co_{0.5}Ni_{0.5}$@SDC), achieving 90% energy efficiency and an operational lifespan of exceeding 2000 hours at a current density of 1 A cm^{-2} during CO_2 to CO conversion at 800 °C (Fig. 10f and g). The catalyst exhibited a 100% CO selectivity and a single-pass conversion of 90%. Its remarkable performance was attributed to the unique encapsulation structure and optimized alloy composition, which together promoted CO_2 adsorption, moderated CO binding, and inhibited metal agglomeration.

In summary, the recent progress in applying Ni-based alloy catalysts to HER, OER, HOR, ORR, and CO_2RR highlights their great potential in electrochemical energy conversion and storage. Compared with monometallic Ni catalysts, Ni-based alloys exhibit significant advantages in electronic structure modulation, intermediate adsorption optimization, active site diversification, and catalytic durability, which collectively account for their enhanced performance in different reaction systems. Notably, the roles of alloying elements in catalytic reactions are not universal but reaction-dependent. In addition, the electrocatalytic behavior of Ni-based alloys is strongly influenced by phase structure, local coordination environment, and surface reconstruction under working conditions, indicating that the real active sites may differ from the initially synthesized structures.

4. Summary and outlook

View Article Online
DOI: 10.1039/D5NR05514H

This review systematically summarizes the latest advances in Ni-based alloy catalysts for synthesis and electrocatalytic applications. The primary synthesis methods include thermal treatment, liquid-phase synthesis, and vapor-phase synthesis. Extensive research has confirmed that regulating synthesis parameters is crucial for precisely controlling the composition, shape, size, structure, and crystal phase of materials, thereby achieving outstanding performance in electrocatalytic applications such as HOR, HER, OER, ORR, and CO_2RR. Despite significant research progress achieved during the past years, further improvements remain needed in realizing robust and reproducible synthesis of Ni-based solid solutions and intermetallic compounds. Moreover, deepening the understanding of their growth mechanisms during synthesis and their highly efficient electrocatalytic mechanisms is also crucial. As such, we highlight the prospects and challenges worthy of attention in the following paragraphs.

(i) Precise and controllable synthesis of Ni-based alloys

Achieving precise control over the composition, structure, and morphology of Ni-based alloys remains a fundamental challenge. Conventional thermal, liquid-phase, and vapor-phase methods often suffer from limitations such as high energy consumption, impurity contamination, or complex parameter control. In particular, for advanced systems such as intermetallic compounds and atomically dispersed alloys, it is still difficult to precisely regulate the spatial distribution and coordination environment of alloying elements. Therefore, developing efficient, green, and highly controllable synthetic strategies, along with quantitative understanding of synthesis parameters, is essential for constructing well-defined catalysts.

(ii) Development of Ni-based high-entropy alloys

Ni-based high-entropy alloys offer unique opportunities due to their tunable multicomponent compositions and potential synergistic effects, and have been extensively explored in recent years.[254] However, a key challenge lies in balancing configurational entropy with catalytic activity and structural stability, as increased compositional complexity may lead to structural instability or poorly defined active sites. Therefore, understanding the fundamental role of each component and achieving controllable entropy-driven catalyst design remain key research directions.

(iii) Developing atomically precise synthesis of single-atom alloys

Ni-based single-atom alloys represent an emerging frontier due to their maximized atom utilization and well-defined active site configurations, in contrast to conventional alloys with less uniform active sites.[255-257] However, the atomically precise synthesis of such alloys remains highly challenging, particularly in achieving uniform dispersion, well-defined coordination environments, and long-term stability of isolated atoms on Ni substrates. Future efforts should focus on achieving atomically precise synthesis and stabilizing isolated active sites under realistic operating conditions.

(iv) Development of sustainable Ni-based alloy catalysts

Despite that Ni-based alloys have emerged as attractive electrocatalysts due to their abundant earth reserves and tunable electronic structures,[15, 21] their sustainability still needs to be addressed. For instance, while the synergistic combination of Ni and Co is widely recognized for enhancing catalytic performance by optimizing intermediate binding energies, the heavy reliance on Co raises significant sustainability concerns because of the high cost, geographical scarcity, and ethical concerns surrounding the extraction of Co.[258-260] The development of Co-free or low-Co-content Ni-based alloys is therefore a vital frontier in creating cost-effective, environmentally friendly energy solutions. At the same time, improving catalyst stability under harsh operating conditions and investigating degradation mechanisms in practical devices are essential for bridging the gap between laboratory research and industrial application.

(v) Machine learning-assisted materials discovery

Machine learning is emerging as a powerful tool for accelerating the development of Ni-based alloy catalysts.[261] It enables efficient screening of complex compositional spaces and facilitates the precise design of composition-structure relationships. In particular, machine learning can be used to predict stable alloy phases, optimize electronic structures, and uncover synergistic effects in multi-element systems. Integrating data-driven approaches with experimental validation will significantly improve the efficiency and rationality of catalyst design.

(vi) In-situ/operando characterization of dynamic active sites

A critical challenge in understanding Ni-based alloy catalysts lies in tracking the dynamic evolution of Ni active sites under operando conditions,[262] especially the continuous changes in their oxidation states and local coordination environments. As known, changes in oxidation states, coordination environments, and surface reconstruction processes directly influence catalytic performance. Advanced in-situ/operando techniques, such as X-ray absorption spectroscopy, Raman spectroscopy, infrared spectroscopy, and TEM, are therefore indispensable for identifying true active species and elucidating reaction mechanisms.

Author contributions

Writing-original draft: Z. Q, Y. J, L. L; writing- review &editing: Z. Q, Y. J, L. L, Q. Y. All authors read and approved the final manuscript.

Conflicts of interest

The authors declare no conflict of interests.

Data availability

This is a review paper and as such it does not include any primary datasets. All the data discussed and analyzed within this review are derived from the published studies and literature references in the manuscript.

DOI: 10.1039/D5NR05514H

Acknowledgements

Z.Q. and Y.J. contributed equally to this work. We acknowledge the supports from Wilson Tang Brilliant Energy Science and Technology Lab (BEST Lab) at the Hong Kong University of Science and Technology (Guangzhou). Q.Y. acknowledges the financial support from Guangdong Basic and Applied Basic Research Foundation (Nos. 2023A1515110010 and 2024A1515012653).

Notes and references

1. R. Eisenberg, H. B. Gray and G. W. Crabtree, *Proc. Natl. Acad. Sci. U. S. A.*, 2020, **117**, 12543-12549.
2. P. Friedlingstein, M. O'Sullivan, M. W. Jones, R. M. Andrew, D. C. E. Bakker, J. Hauck, P. Landschützer, C. Le Quéré, I. T. Luijkx, G. P. Peters, W. Peters, J. Pongratz, C. Schwingshackl, S. Sitch, J. G. Canadell, P. Ciais, R. B. Jackson, S. R. Alin, P. Anthoni, L. Barbero, N. R. Bates, M. Becker, N. Bellouin, B. Decharme, L. Bopp, I. B. M. Brasika, P. Cadule, M. A. Chamberlain, N. Chandra, T. T. T. Chau, F. Chevallier, L. P. Chini, M. Cronin, X. Dou, K. Enyo, W. Evans, S. Falk, R. A. Feely, L. Feng, D. J. Ford, T. Gasser, J. Ghattas, T. Gkritzalis, G. Grassi, L. Gregor, N. Gruber, Ö. Gürses, I. Harris, M. Hefner, J. Heinke, R. A. Houghton, G. C. Hurtt, Y. Iida, T. Ilyina, A. R. Jacobson, A. Jain, T. Jarníková, A. Jersild, F. Jiang, Z. Jin, F. Joos, E. Kato, R. F. Keeling, D. Kennedy, K. Klein Goldewijk, J. Knauer, J. I. Korsbakken, A. Körtzinger, X. Lan, N. Lefèvre, H. Li, J. Liu, Z. Liu, L. Ma, G. Marland, N. Mayot, P. C. McGuire, G. A. McKinley, G. Meyer, E. J. Morgan, D. R. Munro, S. I. Nakaoka, Y. Niwa, K. M. O'Brien, A. Olsen, A. M. Omar, T. Ono, M. Paulsen, D. Pierrot, K. Pocock, B. Poulter, C. M. Powis, G. Rehder, L. Resplandy, E. Robertson, C. Rödenbeck, T. M. Rosan, J. Schwinger, R. Séférian, T. L. Smallman, S. M. Smith, R. Sospedra-Alfonso, Q. Sun, A. J. Sutton, C. Sweeney, S. Takao, P. P. Tans, H. Tian, B. Tilbrook, H. Tsujino, F. Tubiello, G. R. van der Werf, E. van Ooijen, R. Wanninkhof, M. Watanabe, C. Wimart-Rousseau, D. Yang, X. Yang, W. Yuan, X. Yue, S. Zaehle, J. Zeng and B. Zheng, *Earth Syst. Sci. Data*, 2023, **15**, 5301-5369.
3. T. Xia, Q. Ren, J. Yang, Z. Li, M. Shao and X. Duan, *Chem. Res. Chin. Univ.*, 2024, **40**, 577-589.
4. F. Feng, S. Han, Q. Lu and Q. Yun, *Energy Mater. Devices*, 2023, **1**, 9370008.
5. C. Tang, Y. Zheng, M. Jaroniec and S. Z. Qiao, *Angew. Chem., Int. Ed.*, 2021, **60**, 19572-19590.
6. A. Winiwarter, L. Silvioli, S. B. Scott, K. Enemark Rasmussen, M. Sariç, D. B. Trimarco, P. C. K. Vesborg, P. G. Moses, I. E. L. Stephens, B. Seger, J. Rossmeisl and I. Chorkendorff, *Energy Environ. Sci.*, 2019, **12**, 1055-1067.
7. R. Li, K. Xiang, Z. Peng, Y. Zou and S. Wang, *Adv. Energy Mater.*, 2021, **11**, 2102292.
8. Z. W. Seh, J. Kibsgaard, C. F. Dickens, I. Chorkendorff, J. K. Nørskov and T. F. Jaramillo, *Science*, 2017, **355**, eaad4998.
9. Y. Shi, J. Wang, C. Wang, T. T. Zhai, W. J. Bao, J. J. Xu, X. H. Xia and H. Y. Chen, *J. Am. Chem. Soc.*, 2015, **137**, 7365-7370.
10. M. Q. Yang, J. Wang, H. Wu and G. W. Ho, *Small*, 2018, **14**, e1703323.
11. J. Wang, F. Xu, H. Jin, Y. Chen and Y. Wang, *Adv. Mater.*, 2017, **29**, 1605838.
12. M. Gong, W. Zhou, M. C. Tsai, J. Zhou, M. Guan, M. C. Lin, B. Zhang, Y. Hu, D. Y. Wang, J. Yang, S. J. Pennycook, B. J. Hwang and H. Dai, *Nat. Commun.*, 2014, **5**, 4695.
13. M. Gong and H. Dai, *Nano Res.*, 2014, **8**, 23-39.
14. A. G. Oshchepkov, G. Braesch, A. Bonnefont, E. R. Savinova and M. Chatenet, *ACS Catal.*, 2020, **10**, 7043-7068.
15. S. De, J. Zhang, R. Luque and N. Yan, *Energy Environ. Sci.*, 2016, **9**, 3314-3347.
16. M. R. Gennero de Chialvo and A. C. Chialvo, *Electrochim. Acta*, 1988, **33**, 825-830.
17. K. Fominykh, J. M. Feckl, J. Sicklinger, M. Döblinger, S. Böcklein, J. Ziegler, L. Peter, J. Rathousky, E. W. Scheidt, T. Bein and D. Fattakhova Rohlfing, *Adv. Funct. Mater.*, 2014, **24**, 3123-3129.
18. J. W. D. Ng, M. García Melchor, M. Bajdich, P. Chakthranont, C. Kirk, A. Vojvodic and T. F. Jaramillo, *Nat. Energy*, 2016, **1**, 16053.
19. V. Vij, S. Sultan, A. M. Harzandi, A. Meena, J. N. Tiwari, W.-G. Lee, T. Yoon and K. S. Kim, *ACS Catal.*, 2017, **7**, 7196-7225.
20. X. Tian, P. Zhao and W. Sheng, *Adv. Mater.*, 2019, **31**, 1808066.
21. A. Ray, S. Sultana, L. Paramanik and K. M. Parida, *J. Mater. Chem. A*, 2020, **8**, 19196-19245.
22. C. L. Yang, L. N. Wang, P. Yin, J. Liu, M. X. Chen, Q. Q. Yan, Z. S. Wang, S. L. Xu, S. Q. Chu, C. Cui, H. Ju, J. Zhu, Y. Lin, J. Shui and H. W. Liang, *Science*, 2021, **374**, 459-464.
23. F. Feng, C. Ma, S. Han, X. Ma, C. He, H. Zhang, W. Cao, X. Meng, J. Xia, L. Zhu, Y. Tian, Q. Wang, Q. Yun and Q. Lu, *Angew. Chem., Int. Ed. Engl.*, 2024, **63**, e202405173.
24. Y. Yao, Z. Huang, P. Xie, S. D. Lacey, R. J. Jacob, H. Xie, F. Chen, A. Nie, T. Pu, M. Rehwoldt, D. Yu, M. R. Zachariah, C. Wang, R. Shahbazian-Yassar, J. Li and L. Hu, *Science*, 2018, **359**, 1489-1494.
25. Z. P. Wu, S. Shan, Z. H. Xie, N. Kang, K. Park, E. Hopkins, S. Yan, A. Sharma, J. Luo, J. Wang, V. Petkov, L. Wang and C. J. Zhong, *ACS Catal.*, 2018, **8**, 11302-11313.
26. Z. Jia, T. Yang, L. Sun, Y. Zhao, W. Li, J. Luan, F. Lyu, L. C. Zhang, J. J. Kruzic, J. J. Kai, J. C. Huang, J. Lu and C. T. Liu, *Adv. Mater.*, 2020, **32**, 2000385.
27. Y. Yao, Z. Liu, P. Xie, Z. Huang, T. Li, D. Morris, Z. Finfrock, J. Zhou, M. Jiao, J. Gao, Y. Mao, J. J. Miao, P. Zhang, R. Shahbazian Yassar, C. Wang, G. Wang and L. Hu, *Sci. Adv.*, 2020, **6**, eaaz0510.
28. L. Huo, C. Jin, K. Jiang, Q. Bao, Z. Hu and J. Chu, *Adv. Energy Sustainability Res.*, 2022, **3**, 2100189.
29. A. Asghari Alamdari, H. Jahangiri, M. B. Yagci, K. Igarashi, H. Matsumoto, A. Motallebzadeh and U. Unal, *ACS Appl. Energy Mater.*, 2024, **7**, 2423-2435.
30. Y. Liu, H. Hu, K. Wang, J. Huang and D. Wang, *Adv. Energy Mater.*, 2025, **16**, e04101.
31. X. Zhang, Y. Guo and C. Wang, *Energy Mater.*, 2024, **4**, 400044.
32. D. Miao, J. Li, J. Ren and Z. Chen, *Adv. Mater.*, 2026, **38**, e20491.
33. L. An, T. Zhao, W. Lei, C. Yang, J. Yang and D. Wang, *eScience*, 2025, **5**, 100400.
34. Q. Li, Y. Wang, T. Pan, Y. Zhu and H. Pang, *Sci. China Mater.*, 2024, **68**, 317-340.

35. J. Li, L. Li, J. Wang, A. Cabot and Y. Zhu, *ACS Energy Lett.*, 2024, **9**, 853-879.
36. K. X. Du, Y. F. Chen, Z. H. He, P. Fang, C. Ma, N. Fu, Y. Qiu and T. S. Mei, *CCS Chem.*, 2026, **8**, 1204-1225.
37. M. Zhou, C. Li and J. Fang, *Chem. Rev.*, 2021, **121**, 736-795.
38. M. Schalenbach, F. D. Speck, M. Ledendecker, O. Kasian, D. Goehl, A. M. Mingers, B. Breitbach, H. Springer, S. Cherevko and K. J. J. Mayrhofer, *Electrochim. Acta*, 2018, **259**, 1154-1161.
39. L. Rößner, H. Schwarz, I. Veremchuk, R. Zerdoumi, T. Seyller and M. Armbrüster, *ACS Appl. Mater. Interfaces*, 2021, **13**, 23616-23626.
40. S. J. Ji, D. Zhang and N. T. Suen, *Inorg. Chem.*, 2021, **60**, 16754-16760.
41. T. N. Ye, Y. Lu, Y. Kobayashi, J. Li, S. W. Park, M. Sasase, M. Kitano and H. Hosono, *J. Phys. Chem. C*, 2020, **124**, 28589-28595.
42. Z. Chen, H. Yang, S. Mebs, H. Dau, M. Driess, Z. Wang, Z. Kang and P. W. Menezes, *Adv. Mater.*, 2023, **35**, 2208337.
43. H. Shi, T. Y. Dai, X. Y. Sun, Z. L. Zhou, S. P. Zeng, T. H. Wang, G. F. Han, Z. Wen, Q. R. Fang, X. Y. Lang and Q. Jiang, *Adv. Mater.*, 2024, **36**, 2406711.
44. H. Shi, X. Y. Sun, Y. Liu, S. P. Zeng, Q. H. Zhang, L. Gu, T. H. Wang, G. F. Han, Z. Wen, Q. R. Fang, X. Y. Lang and Q. Jiang, *Adv. Funct. Mater.*, 2023, **33**, 2214412.
45. Y. Yang, H. Fei, G. Ruan and J. M. Tour, *Adv. Mater.*, 2015, **27**, 3175-3180.
46. Y. Jin, X. Yue, C. Shu, S. Huang and P. K. Shen, *J. Mater. Chem. A*, 2017, **5**, 2508-2513.
47. S. Ma, X. Wang, X. Zhang, J. Sun, H. Zhang, C. Chen, Y. Han, M. La and X. Li, *Inorg. Chem. Commun.*, 2025, **180**, 114981.
48. H. Zhang, C. Ma, Y. C. Wang, X. Zhu, K. Qu, X. Ma, C. He, S. Han, A. H. Liu, Q. Wang, W. Cao, W. Lin, J. Xia, L. Zhu, L. Gu, Q. Yun, A. L. Wang and Q. Lu, *Angew. Chem. Int. Edit.*, 2024, **63**, e202409515.
49. C. Wu, X. Wang, M. Huang, C. Meng, L. Chang, D. Xu and W. Pei, *Nanoscale*, 2024, **16**, 15148-15157.
50. J. Zhang, T. Wang, P. Liu, Z. Liao, S. Liu, X. Zhuang, M. Chen, E. Zschech and X. Feng, *Nat. Commun.*, 2017, **8**, 15437.
51. Y. Cao, H. Zhang, S. Ji, Z. Sui, Z. Jiang, D. Wang, F. Zaera, X. Zhou, X. Duan and Y. Li, *Angew. Chem. Int. Edit.*, 2020, **59**, 11647-11652.
52. R. Wang, M. Lv, J. Zhang, F. Wang, X. Wang, N. Wang, G. Yu and Z. Zheng, *Chem. Eng. J.*, 2024, **502**, 157981.
53. X. Ge, J. Yin, Z. Ren, K. Yan, Y. Jing, Y. Cao, N. Fei, X. Liu, X. Wang, X. Zhou, L. Chen, W. Yuan and X. Duan, *J. Am. Chem. Soc.*, 2024, **146**, 4993-5004.
54. P. M. Csernica, J. R. McKone, C. R. Mulzer, W. R. Dichtel, H. D. Abruña and F. J. DiSalvo, *ACS Catal.*, 2017, **7**, 3375-3383.
55. L. F. Cabanillas Esparza, E. A. Reynoso Soto, B. Trujillo Navarrete, B. Alcántar Vázquez, C. Silva Carrillo and R. M. Félix-Navarro, *Catalysts*, 2025, **15**, 633.
56. T. Huang, J. Xiao, X. Liu, Y. Feng, J. He, G. Xu and L. Zhang, *Small*, 2025, **21**, e06911.
57. H. Chen, L. Chen and Y. Li, *J. Mater. Chem. A*, 2025, **13**, 35381-35388.
58. O. Johnson, Y. He, I. S. Pierre Charles, J. Richter, B. Joseph and J. N. Kuhn, *ACS Catal.*, 2024, **14**, 7746-7755.
59. J. Ma, F. Xing, Y. Nakaya, K. i. Shimizu and S. Furukawa, *Angew. Chem. Int. Edit.*, 2022, **61**, e202200889.
60. X. Z. Song, D. K. Liu, X. B. Wang, Y. L. Meng, M. Y. Huang, R. C. Zhou, W. T. Zhang, X. F. Wang, L. Z. Liu, J. Liang, Z. Tan and J. Liu, *J. Phys. Chem. Lett.*, 2025, **16**, 9097-9106.
61. F. Zhou, Y. Zhou, Z. Zhang, P. Peng, J. Liang, H. Gao, M. Kang and J. Wang, *Chem. Eng. J.*, 2023, **477**, 146893.
62. D. van den Berg, J. C. Brouwer, R. W. A. Hendrikx and R. Kortlever, *Catal. Today*, 2024, **439**, 114805.
63. R. Kumar, M. Bahri, Y. Song, F. Gonell, C. Thomas, O. Ersen, C. Sanchez, C. Laberty Robert and D. Portehault, *Nanoscale*, 2020, **12**, 15209-15213.
64. J. G. Lee, K. H. Oh, S. W. Kang, J. I. Yang, W. S. Seo and J. C. Park, *Appl. Surf. Sci.*, 2025, **695**, 162936.
65. J. L. Xu, L. L. Li, J. Tang, L. Dai, X. B. Li, Z. G. Ye and J. M. Luo, *J. Alloy. Compd.*, 2021, **865**, 158901.
66. W. Du, W. Zhang, C. Zhu, W. Guo, M. He, H. Zhao and R. Chen, *Coordin. Chem. Rev.*, 2025, **530**, 216473.
67. Y. Chen, J. Liu, Q. Yun, H. Cheng, X. Cui, Z. Fan, L. Fu, C. Gao, J. Ge, Y. Ge, S. Guo, S. Han, X. Hong, B. Huang, H. Huang, X. Huang, X. Huang, X. Liao, C. Ling, D. Liu, Y. Lu, Q. Lu, W. Niu, F. Saleem, M. Shao, Q. Shao, Z. Shi, L. Song, S. Sun, R. D. Tilley, D. Wang, A. L. Wang, J. Wang, P. Xi, Y. Xia, Y. Xiong, N. Yang, P. Yin, Y. Yu, Z. Zhang, M. Zhou, Y. Zhu and H. Zhang, *Chem. Res. Chinese U.*, 2025, **41**, 370-413.
68. Z. Cao, Q. Chen, J. Zhang, H. Li, Y. Jiang, S. Shen, G. Fu, B. a. Lu, Z. Xie and L. Zheng, *Nat. Commun.*, 2017, **8**, 15131.
69. T. Chen, Y. Sun, M. Guo and M. Zhang, *J. Alloys Compd.*, 2018, **766**, 229-240.
70. A. Sajeev, A. Sathyaseelan, K. Serbara Bejigo and S. Jae Kim, *J. Colloid Interf. Sci.*, 2023, **637**, 363-371.
71. Y. Wang, F. Hao, H. Xu, M. Sun, X. Wang, Y. Xiong, J. Zhou, F. Liu, Y. Hu, Y. Ma, X. Meng, L. Guo, C. Wang, M. Shao, G. Wang, J. Wang, P. Lu, J. Yin, J. Wang, W. Niu, C. Ye, Q. Zhang, S. Xi, B. Huang, M. Shao and Z. Fan, *Angew. Chem. Int. Edit.*, 2025, **64**, e202508617.
72. X. Xu, R. Tan, X. Lv, C. Geng, Y. Li, B. Cui and Y. Fang, *Anal. Methods*, 2021, **13**, 5628-5637.
73. G. H. Mohamed Saeed, S. Radiman, S. S. Gasaymeh, H. N. Lim and N. M. Huang, *J. Nanomater.*, 2010, **2010**, 184137.
74. X. Lao, M. Liu and P. Chen, *ACS Appl. Energy Mater.*, 2025, **8**, 6246-6263.
75. Y. Liu, X. Liu, Q. Feng, D. He, L. Zhang, C. Lian, R. Shen, G. Zhao, Y. Ji, D. Wang, G. Zhou and Y. Li, *Adv. Mater.*, 2016, **28**, 4747-4754.
76. J. Li, Z. Luo, Y. Zuo, J. Liu, T. Zhang, P. Tang, J. Arbiol, J. Llorca and A. Cabot, *Appl. Catal. B-Environ.*, 2018, **234**, 10-18.
77. J. Kim, D. W. Kim, J. H. Choi, W. A. Goddard and J. K. Kang, *Proc. Natl. Acad. Sci. USA*, 2025, **122**, e2504226122.
78. D. Wu, W. Zhang and D. Cheng, *ACS Appl. Mater. Interfaces*, 2017, **9**, 19843-19851.
79. A. Halilu, M. D. Hamid, A. A. Umar and M. A. Hashim, *ACS Appl. Mater. Interfaces*, 2025, **17**, 27448-27466.
80. Q. Zhou, Q. Hao, Y. Li, J. Yu, C. Xu, H. Liu and S. Yan, *Nano Energy*, 2021, **89**, 106402.
81. Y. He, Z. Wang, Z. Hu, Y. Hu, X. Fan, S. Liu and C. Wang, *J. Colloid Interf. Sci.*, 2025, **697**, 137911.
82. Q. Zhou, C. Xu, Y. Li, X. Xie, H. Liu and S. Yan, *Sci. China Mater.*, 2022, **65**, 1207-1216.
83. M. Alagesan, M. Mahendran, M. Pandiaraj and N. Rajasekaran, *Nanoscale*, 2025, **17**, 14862-14873.
84. R. A. Alsaiari, A. A. Abd Ellah, Z. M. Anwar, S. S. Shata, M. M. Kamel and N. Y. Mostafa, *RSC Adv.*, 2025, **15**, 22322-22335.

View Article Online
DOI: 10.1039/D5NR05514H

85. Y. Liu, F. Zeng, Y. Kuo, Y. Chen and C. Hsu, *J. Mater. Chem. A*, 2025, **13**, 24062-24072.
86. A. Niciejewska, G. Dercz, I. Matuła, A. Żak, W. Tylus, A. Laszczyńska and J. Winiarski, *Int. J. Hydrogen Energ.*, 2024, **96**, 21-34.
87. J. H. J. Wijten, R. L. Riemersma, J. Gauthier, L. D. B. Mandemaker, M. W. G. M. Verhoeven, J. P. Hofmann, K. Chan and B. M. Weckhuysen, *ChemSusChem*, 2019, **12**, 3491-3500.
88. J. Ren, F. Chen, L. Liu, H. Yang, X. Yan and J. Guo, *Appl. Surf. Sci.*, 2025, **707**, 163593.
89. H. Niu, J. Yuan, Y. Su, L. Ma, S. Xiao, D. Song, X. Xiong, Q. Ren and G. Wang, *J. Colloid Interf. Sci.*, 2025, **698**, 138024.
90. J. Qin, M. Tang, H. Zhang, J. Tian and J. Shen, *J. Colloid Interf. Sci.*, 2025, **699**, 138286.
91. W. Li, Z. Ni, O. Akdim, T. Liu, B. Zhu, P. Kuang and J. Yu, *Adv. Mater.*, 2025, **37**, 2503742.
92. J. M. Costa and A. F. Almeida Neto, *Ultrason. Sonochem.*, 2020, **68**, 105193.
93. A. R. Shetty and A. Chitharanjan Hegde, *Surf. Coat. Technol.*, 2017, **322**, 99-107.
94. B. Li, T. Mei, D. Li and S. Du, *Ultrason. Sonochem.*, 2019, **58**, 104680.
95. S. A. Ataie and A. Zakeri, *Surf. Coat. Tech.*, 2019, **359**, 206-215.
96. A. Bigos, E. Beltowska Lehman, E. García Lecina, M. Bieda, M. J. Szczerba and J. Morgiel, *J. Alloy. Compd.*, 2017, **726**, 410-416.
97. E. Beltowska Lehman, A. Bigos, P. Indyka, A. Chojnacka, A. Drewienkiewicz, S. Zimowski, M. Kot and M. J. Szczerba, *J. Electroanal. Chem.*, 2018, **813**, 39-51.
98. Q. Li, G. Fang, Z. Wu, J. Guo, Y. You, H. Jin and J. Wan, *ChemSusChem*, 2024, **17**, e202301874.
99. M. Smuda, C. Damm, M. Ruck and T. Doert, *ChemistryOpen*, 2020, **9**, 1085-1094.
100. J. Teichert, M. Heise, J. H. Chang and M. Ruck, *Eur. J. Inorg. Chem.*, 2017, **2017**, 4930-4938.
101. J. Dong, X. Liu, N. Lv, H. Li, T. Li, Z. Guo and J. Luo, *J. Alloy. Compd.*, 2024, **992**, 174648.
102. B. M. Thamer, M. M. A. Hameed, H. S. Abdo and M. H. El Newehy, *Ionics*, 2023, **29**, 4203-4215.
103. X. Li, X. Chen, M. Li, H. Wei, X. Yang, S. Ye, L. Li, J. Chen, X. Ren, X. Ouyang, J. Liu, X. Meng, J. Qiu, B. Xiao, Q. Zhang and J. Hu, *Nano-Micro Lett.*, 2025, **17**, 177.
104. L. Jia, R. Luo, X. Zheng, X. Zhang, P. Wang, L. Lv, L. Fu, W. Dong, C. Zhao, D. Li, T. Zhu, Y. Wang, M. Li, J. Li, Y. Yang, D. Kong, J. Liu, Q. Hu, Y. Zhao, Y. Xiong, W. Zhou, J. Zhou and Y. Zhou, *Adv. Funct. Mater.*, 2025, **35**, 2418423.
105. L. Jia, J. Wang, D. Kong, H. Lan, P. Wang, Y. Yang, L. Fu, S. Zheng, X. Huang, Y. Zhou and J. Zhou, *Adv. Funct. Mater.*, 2025, **35**, 2505971.
106. A. Onda, T. Komatsu and T. Yashima, *J. Catal.*, 2001, **201**, 13-21.
107. T. Komatsu, T. Kishi and T. Gorai, *J. Catal.*, 2008, **259**, 174-182.
108. N. U. A. Babar, A. Khan, A. S. Hakeem, H. D. Mohamed, M. H. A. Al Saeed and M. A. Ehsan, *J. Environ. Chem. Eng.*, 2022, **10**, 107959.
109. S. Wang, H. Yan, W. Huo, M. Abdellatief, F. Fang and P. H. C. Camargo, *ACS Appl. Mater. Interfaces*, 2025, **17**, 53587-53599.
110. L. Banko, E. B. Tetteh, A. Kostka, T. H. Piotrowiak, O. A. Krysiak, U. Hagemann, C. Andronescu, W. Schuhmann and A. Ludwig, *Adv. Mater.*, 2023, **35**, 2207635.
111. F. A. A. Nugroho, B. Iandolo, J. B. Wagner and C. Langhammer, *ACS Nano*, 2016, **10**, 2871-2879.
112. Y. Xu, J. Yang, M. Demura, T. Hara, T. Hirano, Y. Matsushita, M. Tanaka and Y. Katsuya, *Appl. Catal. A-Gen.*, 2014, **478**, 165-174.
113. Y. Xu, J. Yang, M. Demura, T. Hirano, Y. Matsushita, M. Tanaka and Y. Katsuya, *Int. J. Hydrogen Energ.*, 2014, **39**, 13156-13163.
114. Y. Xu, H. Jin, T. Hirano, Y. Matsushita and J. Zhang, *Sci. Technol. Adv. Mat.*, 2019, **20**, 622-631.
115. H. Mitani, Y. Xu, T. Hirano, M. Demura and R. Tamura, *Catal. Today*, 2017, **281**, 669-676.
116. D. Garstenauer, P. Guggenberger, O. Zobač, F. Jirsa and K. W. Richter, *Nanoscale*, 2024, **16**, 20168-20181.
117. T. Löffler, H. Meyer, A. Savan, P. Wilde, A. Garzón Manjón, Y.-T. Chen, E. Ventosa, C. Scheu, A. Ludwig and W. Schuhmann, *Adv. Energy Mater.*, 2018, **8**, 1802269.
118. A. Liang, D. C. Goodelman, A. M. Hodge, D. Farkas and P. S. Branicio, *Acta Mater.*, 2023, **257**, 119163.
119. B. Cai, X. Chen, L. Wang and H. Fu, *ACS Catal.*, 2024, **14**, 13602-13629.
120. Y. Men, Y. Tan, P. Li, Y. Jiang, L. Li, X. Su, X. Men, X. Sun, S. Chen and W. Luo, *Angew. Chem., Int. Ed.*, 2024, **63**, e202411341.
121. X. Zhao, X. Li, L. An, K. Iputera, J. Zhu, P. Gao, R. S. Liu, Z. Peng, J. Yang and D. Wang, *Energy Environ. Sci.*, 2022, **15**, 1234-1242.
122. Y. Yang, C. R. Peltier, R. Zeng, R. Schimmenti, Q. Li, X. Huang, Z. Yan, G. Potsi, R. Selhorst, X. Lu, W. Xu, M. Tader, A. V. Soudackov, H. Zhang, M. Krumov, E. Murray, P. Xu, J. Hitt, L. Xu, H. Y. Ko, B. G. Ernst, C. Bundschu, A. Luo, D. Markovich, M. Hu, C. He, H. Wang, J. Fang, R. A. DiStasio, Jr., L. F. Kourkoutis, A. Singer, K. J. T. Noonan, L. Xiao, L. Zhuang, B. S. Pivovar, P. Zelenay, E. Herrero, J. M. Feliu, J. Suntivich, E. P. Giannelis, S. Hammes Schiffer, T. Arias, M. Mavrikakis, T. E. Mallouk, J. D. Brock, D. A. Muller, F. J. DiSalvo, G. W. Coates and H. D. Abruna, *Chem. Rev.*, 2022, **122**, 6117-6321.
123. E. S. Davydova, S. Mukerjee, F. Jaouen and D. R. Dekel, *ACS Catal.*, 2018, **8**, 6665-6690.
124. J. K. Nørskov, T. Bligaard, A. Logadottir, J. R. Kitchin, J. G. Chen, S. Pandelov and U. Stimming, *J. Electrochem. Soc.*, 2005, **152**, J23-J26.
125. W. Liang, Z. Dan, X. Gong, J. Xu, H. Wang, Y. Cao, H. Yu, Y. Jin and H.-F. Wang, *Appl. Catal., B: Environ. Energy*, 2026, **383**, 126069.
126. E. S. Davydova, F. D. Speck, M. T. Y. Paul, D. R. Dekel and S. Cherevko, *ACS Catal.*, 2019, **9**, 6837-6845.
127. X. Tian, J. Liu, P. Zhao, X. Li, Z. Li and W. Sheng, *ChemSusChem*, 2025, **18**, e202402150.
128. S. Lu, J. Pan, A. Huang, L. Zhuang and J. Lu, *Proc. Natl. Acad. Sci.*, 2008, **105**, 20611-20614.
129. E. S. Davydova, J. Zaffran, K. Dhaka, M. C. Toroker and D. R. Dekel, *Catalysts*, 2018, **8**, 454.
130. A. Roy, M. R. Talarposhti, S. J. Normile, I. V. Zenyuk, V. De Andrade, K. Artyushkova, A. Serov and P. Atanassov, *Sustain. Energy & Fuels*, 2018, **2**, 2268-2275.
131. G. Wang, W. Li, B. Huang, L. Xiao, J. Lu and L. Zhuang, *ACS Appl. Mater. Interfaces*, 2019, **2**, 3160-3165.

132. K. Mund, G. Richter and F. von Sturm, *J. Electrochem. Soc.*, 2019, **124**, 1-6.
133. M. H. Tang, C. Hahn, A. J. Klobuchar, J. W. Ng, J. Wellendorff, T. Bligaard and T. F. Jaramillo, *Phys. Chem. Chem. Phys.*, 2014, **16**, 19250-19257.
134. Y. Duan, Z. Y. Yu, L. Yang, L. R. Zheng, C. T. Zhang, X. T. Yang, F. Y. Gao, X. L. Zhang, X. Yu, R. Liu, H. H. Ding, C. Gu, X. S. Zheng, L. Shi, J. Jiang, J. F. Zhu, M. R. Gao and S. H. Yu, *Nat. Commun.*, 2020, **11**, 4789.
135. S. Kabir, K. Lemire, K. Artyushkova, A. Roy, M. Odgaard, D. Schlueter, A. Oshchepkov, A. Bonnefont, E. Savinova, D. C. Sabarirajan, P. Mandal, E. J. Crumlin, Iryna V. Zenyuk, P. Atanassov and A. Serov, *J. Mater. Chem. A*, 2017, **5**, 24433-24443.
136. M. Wang, H. Yang, J. Shi, Y. Chen, Y. Zhou, L. Wang, S. Di, X. Zhao, J. Zhong, T. Cheng, W. Zhou and Y. Li, *Angew. Chem., Int. Ed.*, 2021, **60**, 5771-5777.
137. J. Song, Y. Q. Jin, L. Zhang, P. Dong, J. Li, F. Xie, H. Zhang, J. Chen, Y. Jin, H. Meng and X. Sun, *Adv. Energy Mater.*, 2021, **11**, 2003511.
138. Q. Hu, G. Li, J. Pan, L. Tan, J. Lu and L. Zhuang, *Int. J. Hydrogen Energy*, 2013, **38**, 16264-16268.
139. B. Xiong, W. Zhao, H. Tian, W. Huang, L. Chen and J. Shi, *Chem. Eng. J.*, 2022, **432**, 134189.
140. Y. H. Wang, Y. Yang, F. Y. Gao, X. L. Zhang, L. Zhu, H. K. Yan, P. P. Yang and M. R. Gao, *Angew. Chem., Int. Ed.*, 2024, **63**, e202407613.
141. T. Chen, B. Zhang, X. Yue and S. Huang, *Int. J. Hydrogen Energy*, 2024, **53**, 919-924.
142. W. Sheng, A. P. Bivens, M. Myint, Z. Zhuang, R. V. Forest, Q. Fang, J. G. Chen and Y. Yan, *Energy Environ. Sci.*, 2014, **7**, 1719-1724.
143. Y. Yang, F. Y. Gao, X. L. Zhang, S. Qin, L. R. Zheng, Y. H. Wang, J. Liao, Q. Yang and M. R. Gao, *Angew. Chem., Int. Ed. Engl.*, 2022, **61**, e202208040.
144. S. Qin, Y. Duan, X. L. Zhang, L. R. Zheng, F. Y. Gao, P. P. Yang, Z. Z. Niu, R. Liu, Y. Yang, X. S. Zheng, J. F. Zhu and M. R. Gao, *Nat. Commun.*, 2021, **12**, 2686.
145. X. Wang, X. Liu, J. Fang, H. Wang, X. Liu, H. Wang, C. Chen, Y. Wang, X. Zhang, W. Zhu and Z. Zhuang, *Nat. Commun.*, 2024, **15**, 1137.
146. L. Du, H. Xiong, H. Lu, L. M. Yang, R. Z. Liao, B. Y. Xia and B. You, *Exploration*, 2022, **2**, 20220024.
147. W. Ni, T. Wang, F. Heroguel, A. Krammer, S. Lee, L. Yao, A. Schuler, J. S. Luterbacher, Y. Yan and X. Hu, *Nat. Mater*, 2022, **21**, 804-810.
148. X. L. Zhang, S. J. Hu, Y. H. Wang, L. Shi, Y. Yang and M. R. Gao, *Nano Lett.*, 2023, **23**, 107-115.
149. T. Wang, M. Wang, H. Yang, M. Xu, C. Zuo, K. Feng, M. Xie, J. Deng, J. Zhong, W. Zhou, T. Cheng and Y. Li, *Energy Environ. Sci.*, 2019, **12**, 3522-3529.
150. W. Ni, A. Krammer, C. S. Hsu, H. M. Chen, A. Schuler and X. Hu, *Angew. Chem., Int. Ed.*, 2019, **58**, 7445-7449.
151. F. Y. Gao, S. N. Liu, J. C. Ge, X. L. Zhang, L. Zhu, Y. R. Zheng, Y. Duan, S. Qin, W. Dong, X. Yu, R. C. Bao, P. P. Yang, Z. Z. Niu, Z. G. Ding, W. Liu, S. Lan, M. R. Gao, Y. Yan and S. H. Yu, *Nat. Catal.*, 2022, **5**, 993-1005.
152. W. Yu, J. Liu, H. Hu, Z. He, X. Cui and L. Jiang, *Adv. Funct. Mater.*, 2024, **34**, 2315062.
153. G. Liu, Y. Liu, X. Qiu, B. Zhang, J. Jang, Y. Cui, F. Xiao, Q. Zhao, W. Wang, Y. Kim, W. Xing and M. Shao, *Adv. Energy Mater.*, 2025, **15**, 2405127.
154. G. Xu, J. Li, Y. Zeng, Z. Shi, W. Qi, K. Li, M. Xiao, C. Liu, W. Xing and J. Zhu, *Energy Environ. Sci.*, 2025, **18**, 6273-6282.
155. X. Wang, Y. Zheng, W. Sheng, Z. J. Xu, M. Jaroniec and S.-Z. Qiao, *Mater. Today*, 2020, **36**, 125-138.
156. S. x. Zhang, J. z. Huang, D. j. Ding, J. Tang and X. l. Deng, *Trans. Nonferrous Met. Soc. China*, 2024, **34**, 26-49.
157. M. H. Miles and M. A. Thomason, *J. Electrochem. Soc.*, 2019, **123**, 1459-1461.
158. D. M. Soares, O. Teschke and I. Torriani, *J. Electrochem. Soc.*, 2019, **139**, 98-105.
159. D. Symes, C. Taylor Cox, L. Holyfield, B. Al Duri and A. Dhir, *Mater. Renew. Sustain. Energy*, 2014, **3**, 27.
160. H. R. Pan, Z. Q. Shi, X. Z. Liu, S. Jin, J. Fu, L. Ding, S. Q. Wang, J. Li, L. Zhang, D. Su, C. Ling, Y. Huang, C. Xu, T. Tang and J. S. Hu, *Angew. Chem., Int. Ed.*, 2024, **63**, e202409763.
161. D. E. Brown, M. N. Mahmood, M. C. M. Man and A. K. Turner, *Electrochim. Acta*, 1984, **29**, 1551-1556.
162. I. A. Raj and K. I. Vasu, *J. Appl. Electrochem.*, 1990, **20**, 32-38.
163. M. Urso, N. Gholamiarjenaki, V. Iacono, L. Pulvirenti, A. Scandurra, E. Bruno, G. G. Condorelli and S. Mirabella, *Int. J. Hydrogen Energy*, 2025, **162**, 150722.
164. M. Wang, Z. Wang, X. Yu and Z. Guo, *Int. J. Hydrogen Energy*, 2015, **40**, 2173-2181.
165. J. R. McKone, B. F. Sadtler, C. A. Werlang, N. S. Lewis and H. B. Gray, *ACS Catal.*, 2013, **3**, 166-169.
166. J. Zhang, S. Guo, B. Xiao, Z. Lin, L. Yan, D. Du and S. Shen, *Chem. Eng. J.*, 2021, **416**, 129127.
167. K. Hu, S. Jeong, M. Wakisaka, J.-i. Fujita and Y. Ito, *Metals*, 2018, **8**, 83.
168. P. Shang, Z. Ye, Y. Ding, Z. Zhu, X. Peng, G. Ma and D. Li, *ACS Sustainable Chem. Eng.*, 2020, **8**, 10664-10672.
169. Y. Wang, Y. Sun, F. Yan, C. Zhu, P. Gao, X. Zhang and Y. Chen, *J. Mater. Chem. A*, 2018, **6**, 8479-8487.
170. M. Xia, T. Lei, N. Lv and N. Li, *Int. J. Hydrogen Energy*, 2014, **39**, 4794-4802.
171. W. Gao, W. Gou, X. Zhou, J. C. Ho, Y. Ma and Y. Qu, *ACS Appl. Mater. Interfaces*, 2018, **10**, 1728-1733.
172. J. Panek, J. Kubisztal and B. Bierska ‐ Piech, *Surf. Interface Anal.*, 2014, **46**, 716-720.
173. I. A. Raj and K. I. Vasu, *J. Appl. Electrochem.*, 1992, **22**, 471-477.
174. I. A. Raj, *J. Mater. Sci.*, 1993, **28**, 4375-4382.
175. Y. Zhou, L. Zhao, G. Xu, N. Wang, X. Chen, Z. Wang, D. Kong, X. Yang and C. Meng, *Adv. Energy Mater.*, 2025, **15**, 2501852.
176. J. Zhang, T. Wang, P. Liu, Z. Liao, S. Liu, X. Zhuang, M. Chen, E. Zschech and X. Feng, *Nat. Commun.*, 2017, **8**, 15437.
177. Z. Li, B. Li, M. Yu, C. Yu and P. Shen, *Int. J. Hydrogen Energy*, 2022, **47**, 26956-26977.
178. A. Niciejewska, G. Dercz, I. Matuła, A. Żak, W. Tylus, A. Laszczyńska and J. Winiarski, *Int. J. Hydrogen Energy*, 2024, **96**, 21-34.
179. L. Rossner, H. Schwarz, I. Veremchuk, R. Zerdoumi, T. Seyller and M. Armbruster, *ACS Appl. Mater. Interfaces*, 2021, **13**, 23616-23626.
180. J. H. J. Wijten, R. L. Riemersma, J. Gauthier, L. D. B. Mandemaker, M. Verhoeven, J. P. Hofmann, K. Chan and B. M. Weckhuysen, *ChemSusChem*, 2019, **12**, 3491-3500.
181. W. Du, Y. Shi, W. Zhou, Y. Yu and B. Zhang, *Angew. Chem., Int. Ed.*, 2021, **60**, 7051-7055.

182. R. A. Alsaiari, A. A. Abd Ellah, Z. M. Anwar, S. S. Shata, M. M. Kamel and N. Y. Mostafa, *RSC Adv.*, 2025, **15**, 22322-22335.
183. F. Ning, M. Wang, H. Zhao, G. Ma, J. Meng, R. Dong, H. Hou and X. Wang, *Sustain. Energy & Fuels*, 2024, **8**, 4272-4280.
184. D. Garstenauer, P. Guggenberger, O. Zobac, F. Jirsa and K. W. Richter, *Nanoscale*, 2024, **16**, 20168-20181.
185. D. S. P. Cardoso, S. Eugénio, T. M. Silva, D. M. F. Santos, C. A. C. Sequeira and M. F. Montemor, *RSC Adv.*, 2015, **5**, 43456-43461.
186. G. B. Darband, M. Aliofkhazraei, A. S. Rouhaghdam and M. A. Kiani, *Appl. Surf. Sci.*, 2019, **465**, 846-862.
187. Q. Zhou, Y. Luo, H. Liu, J. Feng, G. Huang, D. Wang and H. Fu, *IOP Conf. Ser.: Earth Environ. Sci.*, 2021, **639**, 012002.
188. N. Loukil and B. Ben Fraj, *Int. J. Hydrogen Energy*, 2025, **147**, 149871.
189. Z. Xie, Y. Zou, L. Deng and J. Jiang, *Adv. Mater. Interfaces*, 2020, **7**, 1901949.
190. P. Zhang, S. Hong, N. Song, Z. Han, F. Ge, G. Dai, H. Dong and C. Li, *Chin. Chem. Lett.*, 2024, **35**, 109073.
191. Z. Qiu, J. Wu, B. Zhang, H. Song, Z. Cui, Z. Liang and L. Du, *Adv. Funct. Mater.*, 2024, **34**, 2408303.
192. Y. Xu, W. Tu, B. Zhang, S. Yin, Y. Huang, M. Kraft and R. Xu, *Adv. Mater.*, 2017, **29**, 1605957.
193. C. Wang, H. Yang, Y. Zhang and Q. Wang, *Angew. Chem., Int. Ed. Engl.*, 2019, **58**, 6099-6103.
194. L. Magnier, G. Cossard, V. Martin, C. Pascal, V. Roche, E. Sibert, I. Shchedrina, R. Bousquet, V. Parry and M. Chatenet, *Nat. Mater.*, 2024, **23**, 252-261.
195. S. Loos, I. Zaharieva, P. Chernev, A. Lissner and H. Dau, *ChemSusChem*, 2019, **12**, 1966-1976.
196. J. Masa and W. Schuhmann, *ChemCatChem*, 2019, **11**, 5842-5854.
197. Y. Matsumoto and E. Sato, *Mater. Chem. Phys.*, 1986, **14**, 397-426.
198. J. Wang and F. Ciucci, *Small*, 2017, **13**, 1604103.
199. Z. Chen, H. Yang, S. Mebs, H. Dau, M. Driess, Z. Wang, Z. Kang and P. W. Menezes, *Adv. Mater.*, 2023, **35**, 2208337.
200. P. W. Menezes, S. Yao, R. Beltran Suito, J. N. Hausmann, P. V. Menezes and M. Driess, *Angew. Chem., Int. Ed.*, 2021, **60**, 4640-4647.
201. W. Zhang, X. He, P. Pan, J. Wang, L. Liu, L. Hou, X. Fan, X. Lu, X. Yu and X. Li, *Energy Environ. Sci.*, 2025, **18**, 8697-8707.
202. Y. Wang, M. Wang, B. Wang, X. Meng, B. Dong, M. Hojamberdiev, Y. Pan, G. Sun, H. Zhang, J. Zeng, M. Wu and H. Hu, *Adv. Funct. Mater.*, 2025, **35**, 2509590.
203. I. Mondal, J. N. Hausmann, G. Vijaykumar, S. Mebs, H. Dau, M. Driess and P. W. Menezes, *Adv. Energy Mater.*, 2022, **12**, 2200269.
204. A. Samanta, S. Das and S. Jana, *Nanoscale Adv.*, 2020, **2**, 417-424.
205. B. M. Jović, U. Č. Lačnjevac, V. D. Jović and N. V. Krstajić, *J. Electroanal. Chem.*, 2015, **754**, 100-108.
206. L. Sharma, N. K. Katiyar, A. Parui, R. Das, R. Kumar, C. S. Tiwary, A. K. Singh, A. Halder and K. Biswas, *Nano Res.*, 2021, **15**, 4799-4806.
207. J. Chen, Y. Ling, X. Yu, G. Wang, L. Huang, A. He, Q. Fan, S. Qin, S. Xiang, M. Xu, Z. Han, J. Du and Q. Xu, *J. Alloys Compd.*, 2022, **929**, 167344.
208. S. Y. Li, T. X. Nguyen, Y. H. Su, C. C. Lin, Y. J. Huang, Y. H. Shen, C. P. Liu, J. J. Ruan, K. S. Chang and J. M. Ting, *Small*, 2022, **18**, e2106127.
209. J. Huang, P. Wang, P. Li, H. Yin and D. Wang, *J. Mater. Sci. Technol.*, 2021, **93**, 110-118.
210. Y. Mei, Y. Feng, C. Zhang, Y. Zhang, Q. Qi and J. Hu, *ACS Catal.*, 2022, **12**, 10808-10817.
211. L. Yi, S. Xiao, Y. Wei, D. Li, R. Wang, S. Guo and W. Hu, *Chem. Eng. J.*, 2023, **469**, 144015.
212. S. Chen, Z. Wang, G. Liu, X. Gao, J. Xiong, Y. Zhao and Y. Li, *J. Colloid Interface Sci.*, 2025, **696**, 137876.
213. M. Du, X. Li, H. Pang and Q. Xu, *EnergyChem*, 2023, **5**, 100083.
214. Z. W. Seh, J. Kibsgaard, C. F. Dickens, I. Chorkendorff, J. K. Norskov and T. F. Jaramillo, *Science*, 2017, **355**, eaad4998.
215. J. Zhu, Z. Fang, X. Yang, M. Chen, Z. Chen, F. Qiu, M. Wang, P. Liu, Q. Xu, X. Zhuang and G. Wu, *ACS Catal.*, 2022, **12**, 6409-6417.
216. J. Y. Zhang, C. Xia, H. F. Wang and C. Tang, *J. Energy Chem.*, 2022, **67**, 432-450.
217. S. Li, L. Shi, Y. Guo, J. Wang, D. Liu and S. Zhao, *Chem. Sci.*, 2024, **15**, 11188-11228.
218. C. Lai, J. Fang, X. Liu, M. Gong, T. Zhao, T. Shen, K. Wang, K. Jiang and D. Wang, *Appl. Catal., B*, 2021, **285**, 119856.
219. M. Wu, B. Guo, A. Nie and R. Liu, *J. Colloid Interface Sci.*, 2020, **561**, 585-592.
220. S. Ci, S. Mao, Y. Hou, S. Cui, H. Kim, R. Ren, Z. Wen and J. Chen, *J. Mater. Chem. A*, 2015, **3**, 7986-7993.
221. Y. Fu, H. Y. Yu, C. Jiang, T. H. Zhang, R. Zhan, X. Li, J. F. Li, J. H. Tian and R. Yang, *Adv. Funct. Mater.*, 2017, **28**, 1705094.
222. J. Huo, L. Lu, Z. Shen, H. Gao and H. Liu, *Surf. Innovations*, 2021, **9**, 37-48.
223. Y. Jiang, P. Ni, C. Chen, Y. Lu, P. Yang, B. Kong, A. Fisher and X. Wang, *Adv. Energy Mater.*, 2018, **8**, 1801909.
224. X. Liu, J. Wang, C. Ma, S. Li, H. Fu, N. Li, Y. Li, X. Fan and W. Peng, *ACS Catal.*, 2025, **15**, 1819-1828.
225. Z. Wang, J. Ang, J. Liu, X. Y. D. Ma, J. Kong, Y. Zhang, T. Yan and X. Lu, *Appl. Catal., B: Environ Energy*, 2020, **263**, 118344.
226. W. Miao, X. Cao, M. Qin, E. Lv, H. Yu, X. Zhang and X. Dong, *Compos. Part B: Eng.*, 2023, **260**, 110769.
227. G. Nam, Y. Son, S. O. Park, W. C. Jeon, H. Jang, J. Park, S. Chae, Y. Yoo, J. Ryu, M. G. Kim, S. K. Kwak and J. Cho, *Adv. Mater.*, 2018, **30**, 1803372.
228. R. He, L. Yang, Y. Zhang, X. Wang, S. Lee, T. Zhang, L. Li, Z. Liang, J. Chen, J. Li, A. Ostovari Moghaddam, J. Llorca, M. Ibáñez, J. Arbiol, Y. Xu and A. Cabot, *Energy Storage Mater.*, 2023, **58**, 287-298.
229. T. Xu, X. Wang, C. Zhao, X. Sheng, N. Wang, Y. Zhao, J. Song, H. Liu, J. Wang and H. Jia, *Appl. Surf. Sci.*, 2025, **697**, 163002.
230. Q. Wang, S. Kaushik, X. Xiao and Q. Xu, *Chem. Soc. Rev.*, 2023, **52**, 6139-6190.
231. S. Chuhadiya, Himanshu, D. Suthar, S. L. Patel and M. S. Dhaka, *Coord. Chem. Rev.*, 2021, **446**, 214115.
232. X. Lu, X. Tan, Q. Zhang, R. Daiyan, J. Pan, R. Chen, H. A. Tahini, D.-W. Wang, S. C. Smith and R. Amal, *J. Mater. Chem. A*, 2019, **7**, 12154-12165.
233. J. Han, X. Bai, X. Xu, X. Bai, A. Husile, S. Zhang, L. Qi and J. Guan, *Chem. Sci.*, 2024, **15**, 7870-7907.
234. S. Jin, Z. Hao, K. Zhang, Z. Yan and J. Chen, *Angew. Chem., Int. Ed.*, 2021, **60**, 20627-20648.

235. H. A. Hansen, J. B. Varley, A. A. Peterson and J. K. Norskov, *J. Phys. Chem. Lett.*, 2013, **4**, 388-392.
236. M. Jia, C. Choi, T. S. Wu, C. Ma, P. Kang, H. Tao, Q. Fan, S. Hong, S. Liu, Y. L. Soo, Y. Jung, J. Qiu and Z. Sun, *Chem. Sci.*, 2018, **9**, 8775-8780.
237. J. R. Kitchin, J. K. Norskov, M. A. Barteau and J. G. Chen, *Phys. Rev. Lett.*, 2004, **93**, 156801.
238. H. Song, Y. C. Tan, B. Kim, S. Ringe and J. Oh, *ACS Appl. Mater. Interfaces*, 2021, **13**, 55272-55280.
239. W. Zhang, J. Zeng, H. Liu, Z. Shi, Y. Tang and Q. Gao, *J. Catal.*, 2019, **372**, 277-286.
240. T. Yue, Y. Chang, J. Liu, J. Jia and M. Jia, *ChemElectroChem*, 2021, **8**, 4233-4239.
241. C. Xu, A. Vasileff, B. Jin, D. Wang, H. Xu, Y. Zheng and S. Z. Qiao, *Chem. Commun.*, 2020, **56**, 11275-11278.
242. F. Liu, C. Wu and S. Yang, *J. Phys. Chem. C*, 2017, **121**, 22139-22146.
243. W. Liu, J. Liu, Y. Yang, B. Xiong and H. Bai, *Fuel*, 2023, **335**, 127026.
244. W. Ma, J. Morales Vidal, J. Tian, M. T. Liu, S. Jin, W. Ren, J. Taubmann, C. Chatzichristodoulou, J. Luterbacher, H. M. Chen, N. Lopez and X. Hu, *Nature*, 2025, **641**, 1156-1161.
245. D. Tan, J. Zhang, X. Cheng, X. Tan, J. Shi, B. Zhang, B. Han, L. Zheng and J. Zhang, *Chem. Sci.*, 2019, **10**, 4491-4496.
246. T. Yang, W. Xie, N. Tian, X. H. Liu and X. Zhang, *J. Alloys Compd.*, 2022, **904**, 164042.
247. Z. Zhong, Y. Tu, L. Zhang, J. Ke, C. Zhong, W. Tan, L. Wang, J. Zhang, H. Song, L. Du and Z. Cui, *ACS Catal.*, 2024, **14**, 2917-2923.
248. W. Xu, H. Chen, K. Jie, Z. Yang, T. Li and S. Dai, *Angew. Chem., Int. Ed. Engl.*, 2019, **58**, 5018-5022.
249. W. Ma, X. He, W. Wang, S. Xie, Q. Zhang and Y. Wang, *Chem. Soc. Rev.*, 2021, **50**, 12897-12914.
250. P. De Luna, C. Hahn, D. Higgins, S. A. Jaffer, T. F. Jaramillo and E. H. Sargent, *Science*, 2019, **364**, eaav3506.
251. S. D. Ebbesen, S. H. Jensen, A. Hauch and M. B. Mogensen, *Chem. Rev.*, 2014, **114**, 10697-10734.
252. S. Wang, H. Tsuruta, M. Asanuma and T. Ishihara, *Adv. Energy Mater.*, 2014, **5**, 1401003.
253. S. Wang, A. Inoishi, J. e. Hong, Y. w. Ju, H. Hagiwara, S. Ida and T. Ishihara, *J. Mater. Chem. A*, 2013, **1**, 12455-12461.
254. P. Ren, T. Gan, J. Cai, J. Hao, Z. Zhuang, C. Jin, W. Zhang, M. Du and H. Zhu, *Angew. Chem., Int. Ed.*, 2025, **64**, e202502776.
255. L. Jiang, D. Tian, G. Deng, J. Cheng, Y. Wang, L. N. Huang, Z. Li, H. Zuo, Y. Li, D. Li, H. Wang and K. Li, *Sci. China Chem.*, 2026, DOI: 10.1007/s11426-026-3417-1.
256. N. Dong, H. Ma and C. Stampfl, *J. Mater. Chem. A*, 2025, **13**, 42247-42256.
257. H. Pan, W. Cai, C. Yang, X. Guan, Y. Wang, X. Cao, J. Ma and J. Zhang, *Nano Lett.*, 2025, **25**, 16919-16927.
258. W. Gong, X. Mao, J. Zhang, Y. Lin, H. Zhang, A. Du, Y. Xiong and H. Zhao, *ACS Nano*, 2023, **17**, 3984-3995.
259. S. Huang, W. Zhang, Q. Chen, S. Zhou, L. Sun, L. Sha, G. Zhuang, P. Wang and X. Han, *Chem. Eur. J.*, 2023, **29**, e202300321.
260. D. Gao, J. Guo, H. He, P. Xiao and Y. Zhang, *Chem. Eng. J.*, 2022, **430**, 133110.
261. T. von Münchow, N. K. Pandit, S. Dana, P. Boos, S. E. Peters, J. Boucat, Y. R. Liu, A. Scheremetjew and L. Ackermann, *Nat. Catal.*, 2025, **8**, 257-269.
262. X. Chen, Y. L. Sun, X. M. Lin, J. C. Dong and J. F. Li, *Nano-Micro Lett.*, 2026, **18**, 170.

View Article Online
DOI: 10.1039/D5NR05514H

Zhongjie Qiu is currently a Ph.D. candidate in the Sustainable Energy and Environment Thrust at the Hong Kong University of Science and Technology (Guangzhou), where he is supervised by Dr. Qinbai Yun. His current research interests include the rational design of metal nanoalloy catalysts and the study of the mechanisms underlying electrocatalytic water splitting and the oxidation of small molecules.

Yuan Jiang is currently a Ph.D. candidate in the Sustainable Energy and Environment Thrust at the Hong Kong University of Science and Technology (Guangzhou). She earned a Bachelor of Science in Applied Chemistry from Chongqing University in 2022 and a Master of Science in Physical Chemistry from Xiamen University in 2025. Her current research focuses on the application of intermetallic compounds in the electrocatalytic conversion of organic compounds.

Lei Li is currently a Postdoctoral Researcher at the thrust of Sustainable Energy and Environment in The Hong Kong University of Science and Technology (Guangzhou), working under the supervision of Dr. Qinbai Yun. He obtained his Ph.D. degree from Shanghai Jiao Tong University in 2025. His current research interests include the rational design of carbon-confined alloy catalysts, mechanistic investigations for the electrocatalytic oxygen reduction reaction (ORR) for hydrogen peroxide (H2O2) synthesis, and the construction of paired electrocatalytic systems.

View Article Online
DOI: 10.1039/D5NR05514H

Qinbai Yun is currently an Assistant Professor in Sustainable Energy and Environment Thrust at The Hong Kong University of Science and Technology (Guangzhou). He obtained his B.E. and M.E. degrees from Tsinghua University, China, and then earned his Ph.D. degree from Nanyang Technological University, Singapore in 2020. After that, he worked as a Postdoc and Research Assistant Professor at City University of Hong Kong and The Hong Kong University of Science and Technology, respectively. His research interests focus on the precise synthesis of low-dimensional metallic materials for applications in electrochemical energy conversion and electrosynthesis of fine chemicals.

View Article Online
DOI: 10.1039/D5NR05514H

This is a review paper and as such it does not include any primary datasets. All the data discussed and analyzed within this review are derived from the published studies and literature references in the manuscript.